



# Prehistoric earthquakes on the Banning strand of the San Andreas fault, North Palm Springs, California

Bryan A. Castillo<sup>1</sup>, Sally F. McGill<sup>1</sup>, Katherine M. Scharer<sup>2</sup>, Doug Yule<sup>3</sup>, Devin McPhillips<sup>2</sup>, James McNeil<sup>3</sup>, Sourav Saha<sup>4</sup>, Nathan D. Brown<sup>4\*</sup>, and Seulgi Moon<sup>4</sup>

<sup>1</sup>Department of Geological Sciences, California State University, San Bernardino, California 92407, USA

<sup>2</sup>Earthquake Science Center, U.S. Geological Survey, Pasadena, California 91106, USA

<sup>3</sup>Department of Geological Sciences, California State University, Northridge, California 91330, USA

<sup>4</sup>Department of Earth, Planetary, and Space Sciences, University of California, Los Angeles, California 90095, USA

## ABSTRACT

We studied a paleoseismic trench excavated in 2017 across the Banning strand of the San Andreas fault and herein provide the first detailed record of ground-breaking earthquakes on this important fault in Southern California. The trench exposed an ~40-m-wide fault zone cutting through alluvial sand, gravel, silt, and clay deposits. We evaluated the paleoseismic record using a new metric that combines event indicator quality and stratigraphic uncertainty. The most recent paleoearthquake occurred between 950 and 730 calibrated years B.P. (cal yr B.P.), potentially contemporaneous with the last rupture of the San Gorgonio Pass fault zone. We interpret five surface-rupturing earthquakes since 3.3–2.5 ka and eight earthquakes since 7.1–5.7 ka. It is possible that additional events have occurred but were not recognized, especially in the deeper (older) section of the stratigraphy, which was not fully exposed across the fault zone. We calculated an average recurrence interval of 380–640 yr based on four complete earthquake cycles between earthquakes 1 and 5. The average recurrence interval is thus slightly less than the elapsed time since the most recent event on the Banning strand. The average recurrence interval on the Banning strand is thus intermediate between longer intervals published for the San Gorgonio Pass fault zone (~1600 yr) and shorter intervals on both the Mission Creek strand of the San Andreas fault (~215 yr) and the Coachella section (~125 yr) of the San Andreas fault.

## INTRODUCTION

The San Andreas fault is the longest fault (~1300 km) and has the highest slip rate of all faults in California. The northern section of the fault ruptured in 1906, and the south-central section ruptured in 1857. Only the southernmost section of the San Andreas fault has not ruptured during the historical record.

The Banning strand of the San Andreas fault is located within a complex portion of the southernmost section of the San Andreas fault zone (Fig. 1).

\*Present address: Department of Earth and Planetary Science, University of California, Berkeley, California 94709, USA

Within the San Gorgonio Pass region, the fault bends to a west-northwest orientation, resulting in a complex zone of transpressional faults (Yule and Sieh, 2003). In addition, faults diverge northward from the southernmost section of the San Andreas fault toward the Eastern California shear zone (Fig. 1). This geometry triggers many questions about the southernmost section of the San Andreas fault system, such as: (1) How is plate-boundary slip accommodated within this region? (2) How have earthquake ruptures in this region made use of the various fault strands within this complex region?

The geometry of the southernmost San Andreas fault becomes more complex from southeast to northwest; the Coachella section is a single strand, but it splits as it approaches the San Bernardino Mountains (Fig. 1). Near Indio, California, the Banning strand diverges from the Mission Creek strand, and farther to the northwest, the Garnet Hill strand deviates from the Banning strand. In the San Gorgonio Pass region, the southernmost San Andreas fault comprises an intricate network of right-lateral, oblique thrust and reverse faults known as the San Gorgonio Pass fault zone (Allen, 1957; Matti et al., 1985; Matti and Morton, 1993; Yule and Sieh, 2003), which connects in turn with the San Bernardino strand of the southernmost San Andreas fault. None of the strands southeast of the San Bernardino section has ruptured in a major earthquake during the historical period, with the exception of the 1986 North Palm Springs earthquake of  $M_w$  6.0, which produced minor fracturing, as discussed below. The Mill Creek strand, which diverges from the Mission Creek strand within the San Gorgonio Pass region, also connects to the San Bernardino strand, but its recency of motion is less clear (cf. Kendrick et al., 2015; Fosdick and Blisniuk, 2018). Given this complexity and limited slip rate data, it is has long been debated whether earthquake ruptures on the southernmost San Andreas fault have propagated through the faults within the San Gorgonio Pass region (Allen, 1957; Yule and Sieh, 2003).

The distribution of slip among various strands of the southernmost San Andreas fault is poorly known. The southeastern portion of the Mission Creek strand seems to accommodate the majority of the slip: The slip rate is 12–22 mm/yr (14–17 mm/yr preferred) at Biskra Palms (Fig. 1; Behr et al., 2010; Fletcher et al., 2010) and is  $21.6 \pm 2$  mm/yr at Pushawalla Canyon (Blisniuk et al., 2021). The slip rate of the Banning strand has been proposed to be 2–6 mm/yr in the Indio Hills (Scharer et al., 2016), and it has been measured

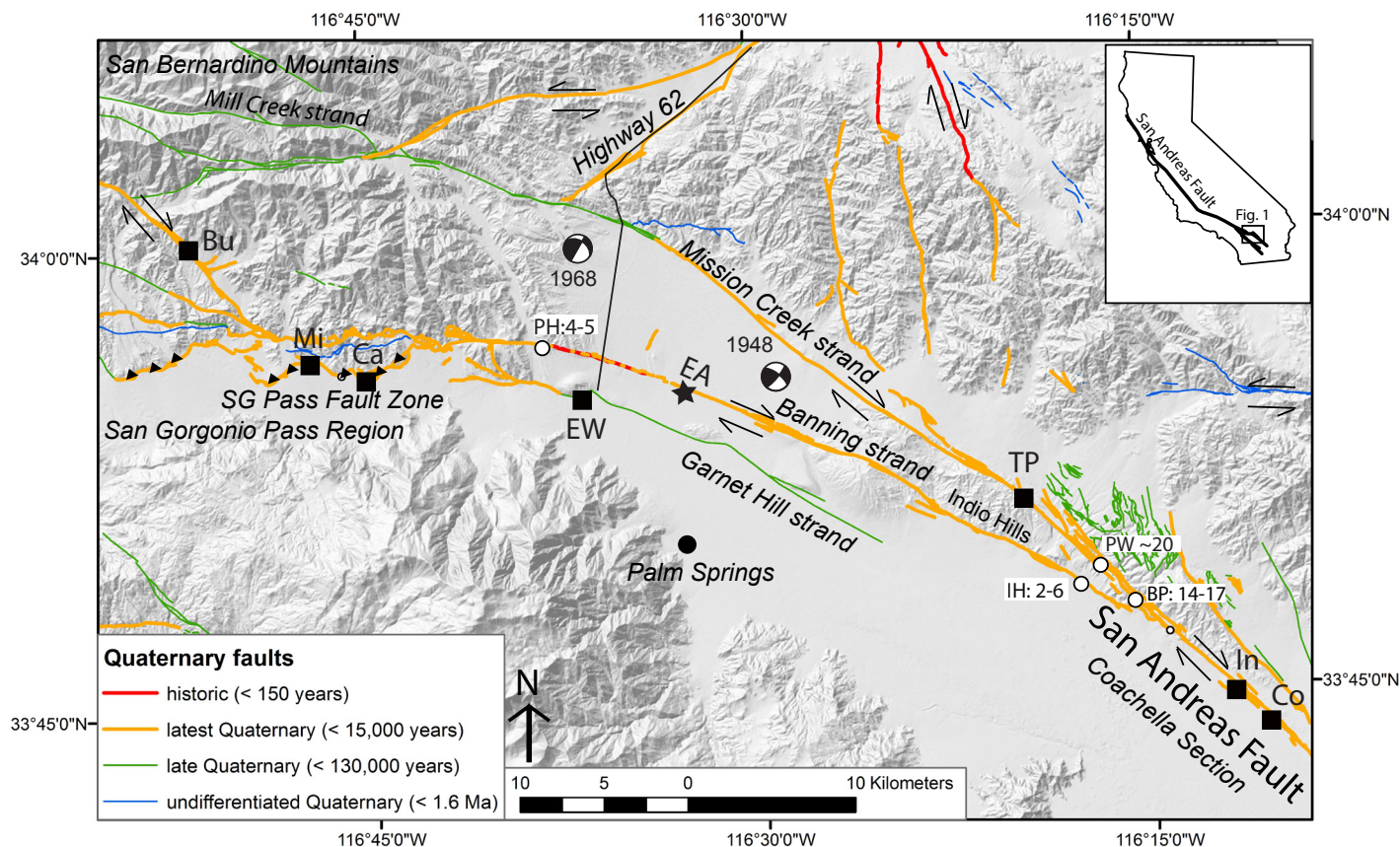


**Figure 1.** Quaternary fault map of the greater San Gorgonio (SG) Pass region in Southern California. Black star shows the location of the 18th Avenue paleoseismic site (EA) on the Banning strand of the southernmost San Andreas fault. Black squares mark the locations of other paleoseismic sites mentioned in the text (Co—Coachella [Philibosian et al., 2011]; In—Indio [Sieh and Williams, 1990]; TP—Thousand Palms [Fumal et al., 2002]; EW—East Whitewater site on the Garnet Hill strand [Cardona, 2016]; Ca—Cabazon [Scharer et al., 2013, abs.; Wolff and Yule, 2014, abs.]; Mi—Millard Canyon [Heermance and Yule, 2017]; Bu—Burro Flats [Yule et al., 2006]). White circles represents slip rate sites mentioned in the text (PH—Painted Hills [Gold et al., 2015]; IH—Indio Hills [Blisniuk et al., 2021]; PW—Pushawalla [Blisniuk et al., 2021]; BP—Biskra Palms [Behr et al., 2010; Fletcher et al., 2010]). Quaternary fault locations and recency of movement are from U.S. Geological Survey and California Geological Survey (2018).

at 2–6 (4–6 preferred) mm/yr at Painted Hills, near Whitewater (Gold et al., 2015). No slip rate estimates are available for the Garnet Hill fault, but it is thought to be an active right-lateral fault based on the presence of uplifted late Quaternary deposits along a series of left-steptovers (Yule and Sieh, 2003; Cardona, 2016).

Although the Mission Creek strand appears to have the highest slip rate of the fault strands in the Coachella Valley, Holocene slip on this fault strand is not established more than a few kilometers northwest of Highway 62 (Fig. 1), and late Quaternary activity on the continuation of this strand is debated

(e.g., Kendrick et al., 2015; Fosdick and Blisniuk, 2018). Instead, slip on the Mission Creek strand has been proposed to transfer northward to the Eastern California shear zone (Nur et al., 1993; Rymer, 1997; Gold et al., 2015), as also suggested by modeling of geodetic data (Meade and Hager, 2005; McCaffrey, 2005; Spinler et al., 2010; McGill et al., 2015).

To better characterize the seismic behavior of the southernmost section of the San Andreas fault, the temporal behavior of these six faults (the Mission Creek, Mill Creek, Banning, Garnet Hill and San Bernardino strands, and the San Gorgonio Pass fault zone) must be examined, including the rate of

ground-rupturing prehistoric earthquakes. This paper contributes the first detailed record of dates of prehistoric earthquakes on the Banning strand.

Two significant historical earthquakes have occurred near the Banning strand of the San Andreas fault: the 1986  $M_w$  6.0 North Palm Springs earthquake and the 1948  $M_w$  6.3 Desert Hot Springs earthquake. Aftershocks of the 1986 event define a nearly planar surface that strikes N60–70°W, is ~15 km in length, dips northeast, and projects to the surface near the Banning strand trace (Nicholson, 1996). The first-motion focal mechanism for the main shock indicates essentially pure right-lateral slip (Nicholson, 1996). Aftershocks of the 1948 event define a plane that strikes N55°W, dips steeply 60° to 70°NE, is ~15 km long, and projects to the surface near the trace of the Banning strand near the northern end of the Indio Hills (Nicholson, 1996). This event was also predominantly right lateral in slip based on focal mechanisms (Nicholson, 1996). From this seismicity, Nicholson (1996) proposed that the Banning strand is nonvertical, is likely segmented according to fault dip as well as fault strike, and was the primary source of both of these recent, moderate-sized earthquakes in the Coachella Valley. A steeper northeastern dip for the Banning strand was modeled from seismic refraction and reflection lines (Fuis et al., 2017).

The 1986 earthquake triggered up to 9 mm of right-lateral slip 44–86 km southeast of the epicenter along the southernmost San Andreas fault (Sharp et al., 1986; Williams et al., 1988). It also produced some ground cracking on the Banning strand between Whitewater River and Highway 62 (Fig. 1), but this was considered to be caused by strong shaking rather than actual surface rupture (Sharp et al., 1986). The 1948 earthquake was very similar to the 1986 earthquake in that they were both initiated at depth, propagated bilaterally, and did not break the surface (Nicholson, 1996).

We report here: (1) the evidence and ages for eight recent paleoearthquakes on the Banning strand; (2) the average recurrence interval between earthquakes on this strand; and (3) a comparison of the timing of paleoearthquakes on the Banning strand with those on the San Geronio Pass fault zone and Mission Creek strand of the San Andreas fault.

## ■ SITE DESCRIPTION

Petra Geosciences excavated a paleoseismic trench on the Banning strand at 18th Avenue, North Palm Springs, California (33.9172°N, 116.538°W). The purpose of the trench was to determine the precise location of Holocene fault strands for the development of the site as required by the Alquist-Priolo Act of 1972. The lead consultant on the trench invited us to conduct a more detailed paleoseismic study on the open trench. The four-tier, benched trench was ~250 m long, ~8 m deep, ~9 m wide at the bottom and ~22 m wide at the ground surface. Most of this study focused on the northern end of the trench (Fig. 2), where an ~40-m-wide fault zone was exposed in interbedded boulder, cobble, gravel, sand, silt, and clay deposits. The trench was excavated into the floodplain of Mission Creek, an ~5-km-wide, broad alluviated surface that slopes gently to the south (Fig. 2, inset).

We observed recent faulting in the northernmost 40 m section of the trench. Five fault strands at the north end of the trench exhibited down-to-the-south faulting, whereas the eight to nine prominent fault strands farther south exhibited down-to-the-north separation (Fig. 3; Plate 1). The fault geometries and thickened section between them are consistent with a pull-apart basin, which likely formed as a result of a small right step in the Banning strand that is evident in publicly available light detection and ranging (lidar) data (Fig. 2; Bevis and Hudnut, 2005; Bevis et al., 2005). The trench configuration produced an asymmetrical exposure of the pull-apart basin because the trench is deepest at the south side of the fault zone and thus reveals older section and more vertical separation across faults. Unfortunately, a fiber-optic line prevented us from extending or deepening the northern end to look for similar relationships there. Although additional secondary faults may exist farther north than at the area excavated, we infer that the exposed pull-apart basin (from about 8 to 28 m) represents the main fault zone because the faults bounding it had the largest vertical displacements (Fig. 3; Plate 1) and the strongest facies changes across these faults (Plate 1), suggesting large strike-slip displacements.

Within the pull-apart basin, 1- to 20-cm-thick layers of very fine sand, silt, and clay were interbedded with coarse sand to granule layers up to 1 m thick. The fine-grained layers were thickest near the center of the pull-apart basin and thinned away from the center. Most of the fine-grained layers either pinched out or gradually became coarse grained within 16–18 m from the center of the basin. A few fine-grained layers extended all the way to the southern end of the section of the trench that was logged (~38–40 m from the center of the basin).

South of the fault zone, the trench was dominated by coarse sand and gravel units ~10–30 cm thick; fine-grained layers were absent, and a few layers contained boulders up to 0.5 m in diameter. Overall, the stratigraphy showed distinct and abrupt contacts between layers and consistent lateral continuity along the trench wall. Locally, and often near fault terminations, upper contacts were scoured and overlain by younger deposits. Our ability to follow contacts through the fault zone was locally restricted by two factors: (1) In places, the vertical separation (and presumably large lateral separation) produced strong changes in the texture of units across the fault zones, and (2) the width of the trench, 9 m at the base and 22 m at the ground surface, made the detailed correlation of strata between the west and east walls of the trench impossible, except for a few prominent layers.

## ■ METHODS

### Field Work

Both the east and west walls of the trench had four vertical tiers ~1.5 m high separated by three horizontal benches (each ~1.5 m in width). We photographed the entire fault zone and used Structure-from-Motion photogrammetric techniques to produce a scaled photomosaic (Plate 1) that we used to log the trench (Fig. 3). Absolute reference frame and scale were determined with a

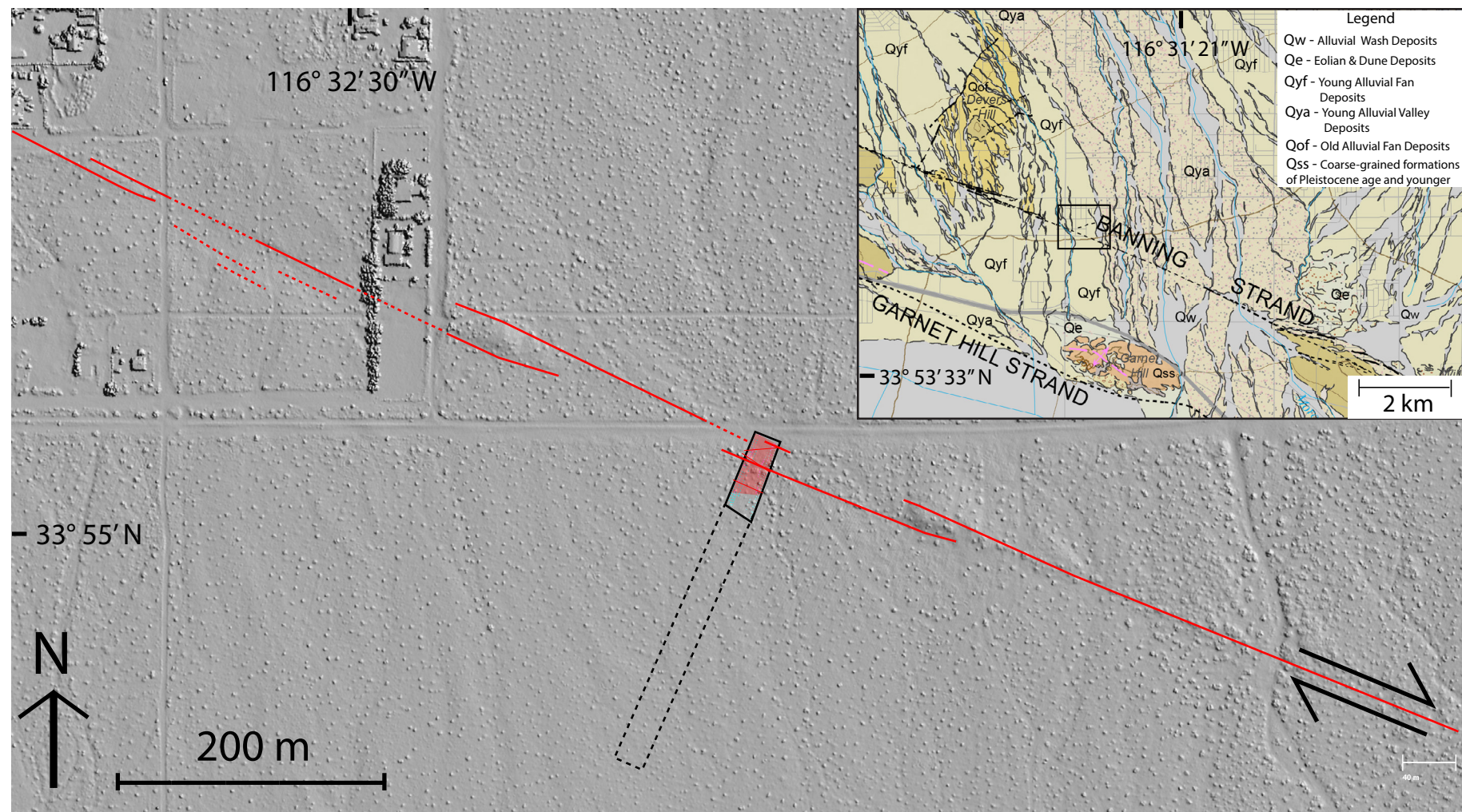
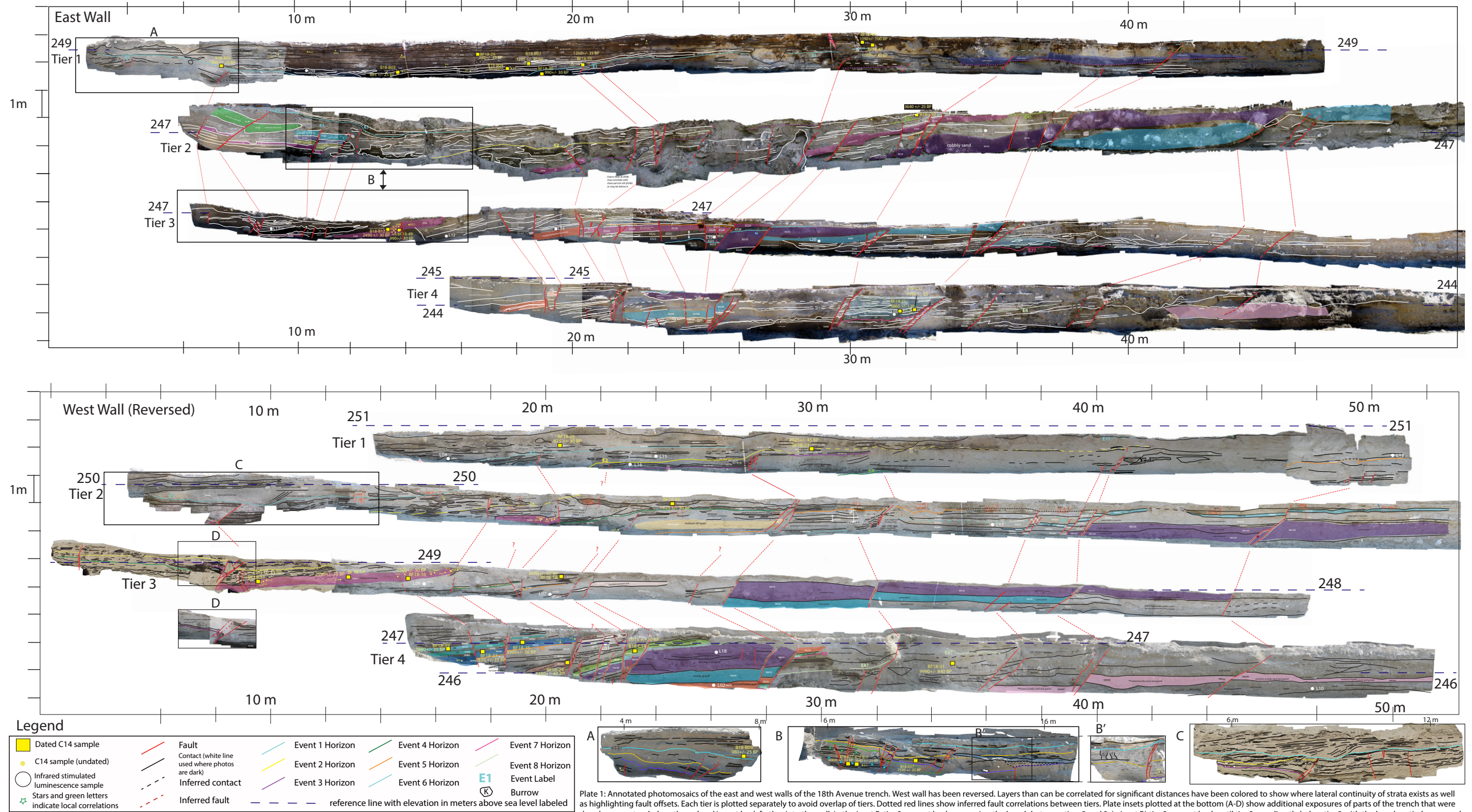


Figure 2. Light detection and ranging (lidar) hillshade image of the Banning strand (Bevis and Hudnut, 2005; Bevis et al., 2005). Fault traces (red lines) based on lidar and historical imagery show alternating steps, with left steps consistent with small pop-up structures. Black solid line shows extent of trench shown in Figure 3 and Plate 1. Within the trench, right-stepping faults are consistent with a pull-apart structure. Red polygon outlines extent of faulting observed in trench. No faults were observed in southern ~160 m of trench (black dashed line). Inset map shows setting of the site on alluvial fans and southward-draining channels (Lancaster et al., 2012).

# Plate 1: 18th Ave Paleoseismic Site Trench Mosaics



To access Plate 1 at full size, please visit <https://doi.org/10.1130/GEOS.S.14098595>.

Plate 1. 18th Avenue paleoseismic site trench mosaics. IRSL—infrared stimulated luminescence.

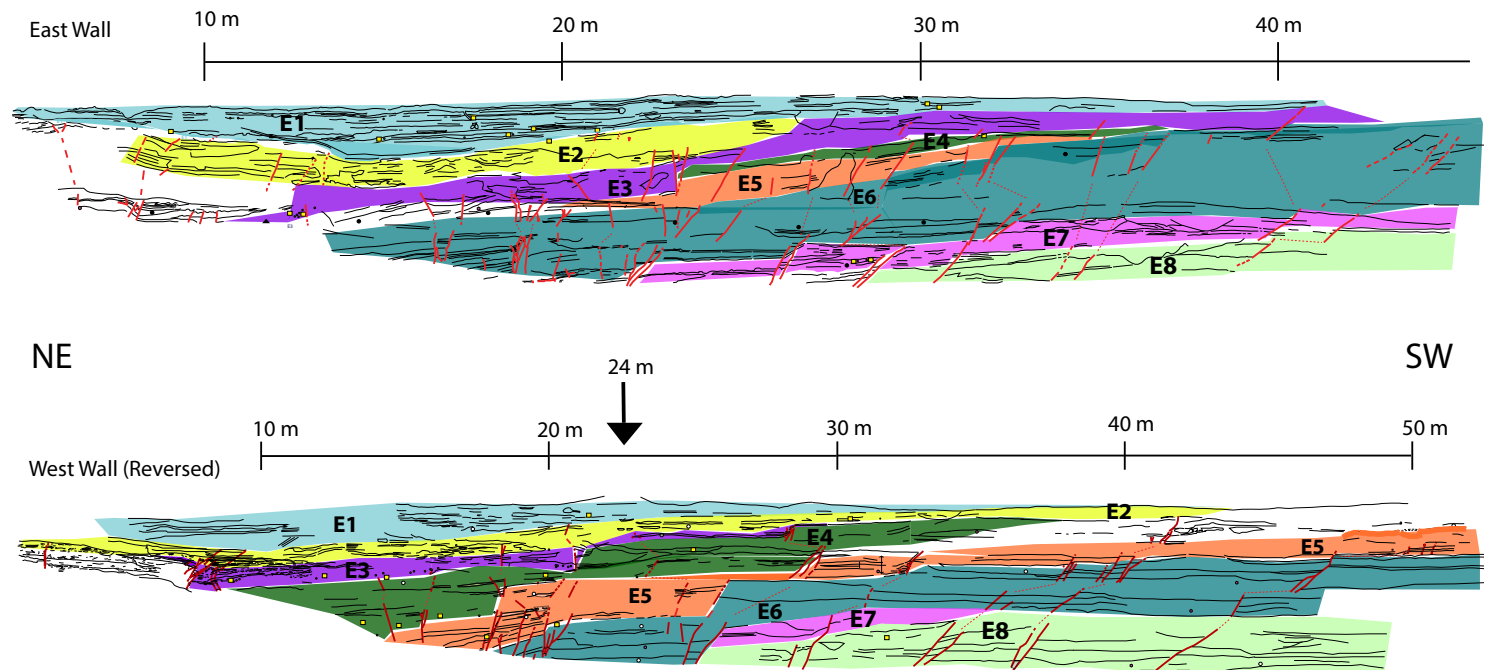


**Figure 3.** Simplified trench diagram to highlight thickness changes and extent of sedimentary packages associated with each earthquake. Each color illustrates the sedimentary packages between two event horizons. For example, the event 1 horizon is at the base of the light blue package labeled “E1.” Benched walls are projected onto a single plane, causing some overlap and omission of units. Red subvertical lines are faults. Dashed thick red lines mark inferred faults in the trench wall. Dashed thin red lines show how faults connect across benches. Small symbols are sample locations, and black lines illustrate contacts between sedimentary layers. Arrow on meter 24 on the west wall locates the type section used to construct the stratigraphic age control column; no vertical exaggeration. E1–E8—earthquake events 1–8.

total station survey of a grid of nails placed ~2 m apart along the top and base of each tier. The photomosaic provided a base for logging of stratigraphic layers and faulting in the field. The final orthomosaic (Plate 1) was rectified using the surveyed nails as control points.

**Dating**

Thirty-three samples of charcoal, typically collected from fine-grained layers, were radiocarbon dated at the Center for Accelerator Mass Spectrometry at Lawrence Livermore National Laboratory to constrain the ages of the prehistoric earthquake horizons. We used the online software OxCal (Bronk Ramsey, 2009) with the IntCal 13 calibration curve (Reimer et al., 2013) to calibrate radiocarbon measurements. The results are listed in Table 1.

In total, 17 samples were collected and dated using post-infrared infrared stimulated luminescence protocol (p-IR IRSL; Buylaert et al., 2009) at the

University of California–Los Angeles Luminescence Laboratory. The equivalent dose ( $D_e$ ) values for individual grains were measured using a modified single-aliquot regenerative (SAR) dose protocol (Wintle and Murray, 2006) and synthesized into sample  $D_e$  values using conventional age models (Galbraith et al., 1999). Post-IR IRSL<sub>225</sub> ages were obtained by dividing  $D_e$  by the geologic dose rate on the DRAC 1.2 online calculator (Durcan et al., 2015). The mean age  $\pm 1\sigma$  uncertainty are reported for all luminescence ages (Table 2). Details of the luminescence dating methods used are provided in the Supplemental Material.<sup>1</sup>

**Recognition of Earthquake Horizons**

A central challenge in paleoseismic investigations is to identify horizons that were at the ground surface when (prehistoric) earthquakes ruptured the fault. Upward termination of fault strands is a common type of evidence for an earthquake horizon. However, upward termination of fault strands alone

1 | Supplementary Information for Castillo et al. (2020): Prehistoric earthquakes on  
 2 | the Banning strand of the San Andreas Fault, <https://doi.org/10.1130/GES02237.1>  
 3 |  
 4 | This supplement provides details of the luminescence dating methods and results, as  
 5 | well as details about each indicator for each paleoseismic event in the 18<sup>th</sup> Avenue  
 6 | trench.  
 7 |  
 8 | DETAILS OF THE LUMINESCENCE DATING METHOD AND RESULTS  
 9 |  
 10 | K-feldspar grains of 175–200  $\mu\text{m}$  diameter were isolated from the sedimentary  
 11 | samples under dim amber LED light conditions. Subsamples were wet-sieved and  
 12 | separated by density with lithium metatungstate ( $\rho < 2.565 \text{ g/cm}^3$ ; Rhodes, 2015).  
 13 | Luminescence measurements were carried out using a TL-DA-20 Rise automated  
 14 | reader equipped with a single-grain IR laser (830 nm, at 90% of 150 mW; Better-Jensen  
 15 | et al., 2003) and a  $^{90}\text{Sr}/^{90}\text{Y}$  beta source. Emissions were detected using a  
 16 | photomultiplier tube with the IRSL signal passing through a Schott BG39–BG39 filter  
 17 | combination. Samples were mounted on aluminum single-grain discs with 100 holes.  
 18 | The gamma dose-rate was measured in situ using a calibrated, portable NaI gamma  
 19 | spectrometer, except for one sample (L11).  
 20 | The U and Th concentrations were measured with inductively-coupled plasma  
 21 | mass spectrometry (ICP-MS), and the K concentration was measured using inductively-  
 22 | coupled plasma optical emission spectrometry (ICP-OES). These values were used to  
 23 | calculate the total beta dose rate contribution using the conversion factors of Liritzis et

<sup>1</sup>Supplemental Material. Details of luminescence methods and results, and table of event indicators. Please visit <https://doi.org/10.1130/GEOS.S.14098589> to access the supplemental material, and contact editing@geosociety.org with any questions.

TABLE 1. RADIOCARBON DATES FOR 18TH AVENUE TRENCH SAMPLES

CAMS no.*	Original sample name	Simplified sample name	$\delta^{13}\text{C}^{\dagger}$ (‰)	Fraction modern <sup>§</sup>	$\delta^{14}\text{C}^{\ddagger}$ (‰)	<sup>14</sup> C age <sup>§</sup> (yr B.P.)	Calibrated ages (B.C./A.D.)			Calibrated ages (yr B.P.)		Sample location	Tier	Meter
							From	To	%	From	To			
176783	BF18-46	A46	-25	0.8731 ± 0.0105	-126.9 ± 10.5	1090 ± 100	693	1155	95.4	1257	795	East wall	1	29.2
176781	BF18-29	A29	-25	0.9708 ± 0.0038	-29.2 ± 3.8	240 ± 35	1522	—	95.4	428	—	East wall	1	17.3
176782	BF18-47	A47	-25	0.8741 ± 0.0046	-125.9 ± 4.6	1080 ± 45	779	1030	95.4	1171	920	East wall	1	29.5
177821	B18-B09	B09	-21.3	0.8853 ± 0.0026	-114.7 ± 2.6	980 ± 25	996	1154	95.4	954	796	East wall	1	9
177818	B18-B07	B07	-24.2	0.8606 ± 0.0038	-139.4 ± 3.8	1205 ± 40	688	945	95.4	1262	1005	East wall	1	19
177819	B18-B03	B03	-22.5	0.8956 ± 0.0026	-104.4 ± 2.6	885 ± 25	1045	1218	95.4	905	732	East wall	1	15
177820	B18-B04	B04	-25.7	1.0921 ± 0.0032	92.1 ± 3.2	>Modern ± N.A.#	1896	1904	95.4	54	46	East wall	1	18
176784	BF18-55	A55	-25	0.8602 ± 0.0033	-139.8 ± 3.3	1210 ± 35	689	938	95.4	1261	1012	East wall	1	20.4
176785	BF18-25	A25	-25.5	0.9201 ± 0.0027	-79.9 ± 2.7	670 ± 25	1276	1390	95.4	674	560	West wall	1	20.5
176786	BF18-30	A30	-24.2	0.8832 ± 0.0027	-116.8 ± 2.7	1000 ± 25	987	1149	95.4	963	801	East wall	1	19.3
176787	BF18-53	A53	-25	0.7773 ± 0.0043	-222.7 ± 4.3	2025 ± 45	-165	66	95.4	2115	1884	West wall	1	29
176788	BF18-11	A11	-22.7	0.7258 ± 0.0024	-274.2 ± 2.4	2575 ± 30	-811	-569	95.4	2761	2519	West wall	3	9.8
176789	BF18-14	A14	-24.0	0.7238 ± 0.0024	-276.2 ± 2.4	2595 ± 30	-825	-599	95.4	2775	2549	West wall	3	13
176790	BF18-49	A49	-24.2	0.7265 ± 0.0025	-273.5 ± 2.5	2565 ± 30	-806	-556	95.5	2756	2506	East wall	3	14.5
176791	BF18-16	A16	-25.4	0.7328 ± 0.0022	-267.2 ± 2.2	2495 ± 25	-773	-540	95.4	2723	2490	West wall	3	15
177825	B18-B12	B12	-23.9	0.7334 ± 0.0023	-266.6 ± 2.3	2490 ± 30	-781	-511	95.4	2731	2461	East wall	3	14
176792	BF18-44	A44	-22.6	0.7948 ± 0.0021	-205.2 ± 2.1	1845 ± 25	87	238	95.4	1863	1712	West wall	2	23.5
177826	B18-C10	C10	-25.0	0.6357 ± 0.0020	-364.3 ± 2.0	3640 ± 25	-2130	-1926	95.4	4080	3876	East wall	2	32.5
176793	BF18-18	A20	-25	0.7341 ± 0.0051	-265.9 ± 5.1	2480 ± 60	-777	-416	95.4	2727	2366	West wall	3	20
176794	BF18-39	A39	-25	0.6170 ± 0.0026	-383.0 ± 2.6	3880 ± 35	-2469	-2212	95.4	4419	4162	West wall	4	16
177829	BF18-33	A33	-25	0.6207 ± 0.0025	-379.3 ± 2.5	3830 ± 35	-2457	-2150	95.4	4407	4100	West wall	4	18
177830	BF18-35	A35	-20.6	0.6082 ± 0.0019	-391.8 ± 1.9	3995 ± 30	-2576	-2467	95.4	4526	4417	West wall	4	19.5
177849	BF 18-24	A24	-25	0.5826 ± 0.0027	-417.4 ± 2.7	4340 ± 40	-3086	-2890	95.4	5036	4840	West wall	4	20.5
177833	B18-C14	C14	-24.0	0.4176 ± 0.0016	-582.4 ± 1.6	7015 ± 30	-5987	-5840	95.4	7937	7790	West wall	4	23
176795	BF18-21	A21	-25	0.2932 ± 0.0040	-706.8 ± 4.0	9860 ± 120	-9859	-8855	95.4	11,809	10,805	East wall	4	31
177834	B18-C12	C12	-22.7	0.3030 ± 0.0009	-697.0 ± 0.9	9590 ± 25	-9151	-8823	95.4	11,101	10,773	East wall	4	32.5
176796	BF18-31	A31	-25	0.2885 ± 0.0299	-711.5 ± 29.9	9990 ± 840	-11,810	-7519	95.4	13,760	9469	West wall	4	34
177822	B18-B18	B18	-25	0.7723 ± 0.0049	-227.7 ± 4.9	2080 ± 60	-352	55	95.4	2302	1895	East wall	2	12
177823	B18-C01	C01	-26.7	0.7833 ± 0.0023	-216.7 ± 2.3	1960 ± 25	-38	115	95.4	1988	1835	East wall	1-2	N.A.#
177824	BF18-57	A57	-21.9	0.7244 ± 0.0021	-275.6 ± 2.1	2590 ± 25	-811	-767	95.4	2761	2717	East wall	3	10
177827	B18-B11	B11	-23.7	0.6371 ± 0.0022	-362.9 ± 2.2	3620 ± 30	-2118	-1984	95.4	4068	3934	East wall	3B	14.5
177828	B18-B10	B10	-25	0.6381 ± 0.0026	-361.9 ± 2.6	3610 ± 35	-2120	-1885	95.4	4070	3835	East wall	3B	14.5
177831	B18-B16	B16	-22.0	0.6201 ± 0.0019	-379.9 ± 1.9	3840 ± 25	-2456	-2203	95.4	4406	4153	East wall	3	7
177832	B18-B17	B17	-25	0.6226 ± 0.0026	-377.4 ± 2.6	3805 ± 35	-2435	-2136	95.4	4385	4086	East Wall	3	7

Note: Samples from 18th Avenue paleoseismic trench, North Palm Springs, California (33.9172°N, 116.538°W). Sample preparation backgrounds have been subtracted based on measurements of samples of <sup>14</sup>C-free coal. Backgrounds were scaled relative to sample size. Error is large on 176796 in part due to the age of sample (nearly two half lives), even though the target was 110 µg C.

\*CAMS—Center for Accelerator Mass Spectrometry sample number. CAMS 176783 and 176795 were <30 µg C samples.

<sup>†</sup> $\delta^{13}\text{C}$  values are the assumed values according to Stuiver and Polach (1977) when given without decimal places. Values measured for the material itself are given with a single decimal place.

<sup>§</sup>Radiocarbon concentration is given as fraction modern,  $\delta^{14}\text{C}$ , and conventional radiocarbon age. The quoted age is in radiocarbon years before present using the Libby half life of 5568 yr and following the conventions of Stuiver and Polach (1977).

#N.A.—not available.

TABLE 2. DOSE-RATE INFORMATION AND POST-IR IRSL AGES FOR 18TH AVENUE TRENCH SAMPLES

Lab code	Field code	Unit	Depth (m)	K* (%)	Th* (ppm)	U* (ppm)	Measured gamma dose rate <sup>†</sup> (Gy/k.y.)	Total dose rate (Gy/k.y.)	Equivalent dose (Gy)	Post-IR IRSL age <sup>§,¶</sup> (ka)
J1284	L01 (BF17-01)	W570	3.8	2.8	19.2	3.28	1.993 ± 0.004	6.011 ± 0.26	21.69 ± 2.2	3.61 ± 0.4
J1285	L02 (BF17-02)	W670	4.9	2.7	18.1	2.56	1.897 ± 0.004	5.466 ± 0.23	29.29 ± 2.15	5.36 ± 0.45
J1286	L03 (BF17-03)	E690	5.1	2.7	16.3	2.65	1.709 ± 0.004	5.037 ± 0.213	31.82 ± 1.16	6.32 ± 0.35
J1287	L04 (BF17-04)	E630	3.5	2.8	15.9	2.57	1.944 ± 0.005	5.487 ± 0.229	28.31 ± 3.6	5.16 ± 0.69
J1288	L05 (BF17-05)	E510	2.6	2.7	21.6	2.78	2.458 ± 0.005	6.372 ± 0.265	31.93 ± 1.76	5.01 ± 0.35
J1289	L06 (BF17-06)	W320	2.9	2.7	17.3	2.46	1.925 ± 0.004	5.69 ± 0.243	13.12 ± 1.78	2.31 ± 0.33
J1290	L07 (BF17-07)	W540C	3.2	2.8	18.7	2.97	1.931 ± 0.004	5.899 ± 0.255	17.19 ± 1.71	2.91 ± 0.32
J1291	L08 (BF17-08)	W82B	0.8	2.7	18.5	2.44	1.891 ± 0.004	5.702 ± 0.242	4.04 ± 0.69	0.71 ± 0.13
J1292	L09 (BF17-09)	E40	0.8	2.9	15.1	2.51	1.716 ± 0.004	5.074 ± 0.214	4.29 ± 0.51	0.85 ± 0.11
J1293	L10 (BF17-10)	W860	6	2.6	19.3	2.46	1.946 ± 0.004	5.542 ± 0.234	39.00 ± 3.12	7.04 ± 0.64
J1294	L11 (BF17-11)	E260	3	2.8	13.8	2.02	N/A ± N/A**	5.212 ± 0.233	9.84 ± 0.57	1.89 ± 0.14
J1394	L15 (BF17-15)	W150E	0.8	2.5	16.1	2.17	1.922 ± 0.005	4.879 ± 0.199	6.59 ± 1.03	1.35 ± 0.22
J1395	L16 (BF17-16)	W220E	1.3	2.8	18.3	2.91	1.874 ± 0.004	5.904 ± 0.256	9.82 ± 1.18	1.66 ± 0.21
J1396	L17 (BF17-17)	W602C	2.4	2.3	16.9	2.73	2.004 ± 0.005	5.517 ± 0.228	28.37 ± 2.84	5.14 ± 0.56
J1397	L18 (BF17-18)	W610	4	2.5	16.3	2.09	1.971 ± 0.005	5.054 ± 0.206	28.74 ± 3.04	5.69 ± 0.64
J1398	L19 (BF17-19)	E525	3.6	2.5	17.5	2.71	2.111 ± 0.005	5.084 ± 0.208	20.55 ± 2.78	4.04 ± 0.57
J1399	L20 (BF17-20)	E620	3.7	2.4	17.4	2.71	1.89 ± 0.005	5.297 ± 0.219	26.03 ± 2.94	4.91 ± 0.59

Location: 33.9174°E, 116.5389°W, 247 m above sea level.

Note: Grain size used was 175–200 µm. Radionuclide conversion factor is after Liritzis et al. (2013);  $\alpha$  attenuation factor is after Brennan et al. (1991);  $\beta$  attenuation factor is after Guerin et al. (2012). Internal K contents were 12.5% ± 0.5% after Huntley and Baril (1997). Cosmic dose rates followed Prescott and Hutton (1994). Post-IR IRSL—post-infrared infrared stimulated luminescence.

\*U, Th, and K contents were derived via inductively coupled plasma—optical emission spectrometry (ICP-OES) with relative uncertainties of 5%.

<sup>†</sup>Gamma dose rate derived from in situ gamma spectrometry.

<sup>§</sup>Ages were calculated in DRAC calculator (Durcan et al., 2015).

<sup>¶</sup>No fading was observed. Errors are reported as 1 $\sigma$ .

\*\*N.A.—not available.

does not always provide a reliable indicator of the stratigraphic position of an earthquake horizon because fault strands with small displacements may not necessarily have ruptured all the way to the ground surface at the time of an event (e.g., Bonilla and Lienkaemper, 1991). Earthquake horizons are considered more reliable if a sedimentary response to the displacement is preserved (e.g., Scharer et al., 2017; Onderdonk et al., 2018). For example, when a graben or uphill-facing fault scarp is formed, it may create a closed depression where water will pond and deposit fine-grained material in the depression. In this configuration, the fault scarp may be preserved and buried by the fine-grained sediments, which generally thin and pinch out at the edges of the depression that formed as a result of vertical separation at the surface. Thus, both the fault strand and the subsequent depositional record provide more robust evidence of the paleoearthquake horizon than simple upward termination alone.

At the 18th Avenue trench, most of the exposed fault strands accommodate a component of down-to-the-north displacement. Given the southward slope of the floodplain of Mission Creek, down-to-the-north displacement on individual fault strands created uphill-facing scarps and ponding of fine-grained

sediments. Thinning of fine-grained layers across the scarps that filled fault-bounded depressions provided strong evidence for some of the earthquake horizons at the site.

### Event Indicator Quality Ranking

At the 18th Avenue trench, we found evidence for eight paleoearthquake horizons with varying quality. To compare the strength of evidence for the different events, we used a ranking scale to classify each of the indicators based on the quality of structural and sedimentological evidence used to identify the stratigraphic level that was at the ground surface at the time of the event. Each event indicator was given a quality rank on a scale of 0 to 5, with higher numbers representing more reliable evidence (Table 3). Table 3 was developed based on a table previously published in Scharer et al. (2017), with several modifications that tailored the criteria to the 18th Avenue trench. Because of unique considerations related to local geology and fault zone architecture, there are always a certain number of site-specific decisions/adjustments that must be made.



TABLE 3. DESCRIPTION OF EVENT INDICATORS AND ASSOCIATED QUALITY RANKING

Quality	Description
0	<p>Fault tip where upward termination is not distinct due to unclear stratigraphy, resulting in uncertainty as to the event during which this fault slipped, with no preferred event horizon among the possibilities.</p> <p>Fault tip has distinct upward termination, but the event with which it is associated remains unclear because the fault terminates upward at a scoured contact that erodes through one or more event horizons.</p>
1	<p>Fault has minor offset (&lt;5 cm), even if the upward termination is distinct.</p> <p>Fault has moderate offset but indistinct upward termination, allowing multiple interpretations for the event horizon during which this fault slipped. Nonetheless, there is reason to prefer association of this indicator with one of these event horizons over the others.</p> <p>Minor or gradual thickness changes occur across fault that could simply reflect depositional gradients rather than filling of earthquake-produced depression.</p> <p>Folding amplitude is small, and thickness change above horizon of folding is moderate, but stratigraphic location of the lowest unfolded layers is indistinct enough to allow for multiple interpretations for the event horizon during which this folding occurred.</p> <p>Nonetheless, there is reason to prefer one of these event horizons over the others.</p> <p>Possible fissure is observed that could alternatively be interpreted as shear of a massive layer disrupted by multiple fault strands.</p>
2	<p>Fault has moderate offset (<math>\geq 5</math> cm) and indistinct upward termination, but the indicator can still be clearly associated with one event horizon.</p> <p>Folding amplitude is small, and thickness change above horizon of folding is moderate.</p>
3	<p>Fault tip has distinct upward termination and moderate offset (<math>\geq 5</math> cm).</p> <p>Folding and thickness changes in layers above folding horizon are substantial (<math>\sim 20</math> cm), but folding horizon has no clearly causative fault, and (or) the horizon of folding is difficult to discern.</p> <p>Possible fissure is observed for which the fill material does not clearly postdate the inferred event horizon, and both walls of the fissure are faults that have reruptured in a younger event.</p>
4	<p>Fault tip is associated with a colluvial wedge or layer thickness changes that reflect modification or erosion of scarp.</p> <p>Possible fissures are observed for which the fill material does not clearly postdate the inferred event horizon, but at least one wall of the fissure is a fault with a distinct upward termination, which has not reruptured in a younger event.</p> <p>Broad warping and large thickness changes in the layer above the folding horizon indicate rapid filling of a depression closely related to the fault that moved to provide accommodation space.</p>
5	<p>Fissures are clearly filled with material that postdates the inferred event horizon.</p> <p>Folding and growth strata occur in which it is clear that the topography was rapidly filled by a single sedimentation event, and event horizon has a causal fault.</p>

*Note:* Table is modified from Scharer et al. (2017) to reflect the depositional characteristics of the 18th Avenue site.

First, it is common for faults that slipped with minor displacement to terminate upward at different stratigraphic levels because some of the strands did not rupture all the way to the surface (Bonilla and Lienkaemper, 1991; Weldon et al., 2002). Because of this, Scharer et al. (2017) made a distinction between faults with minor offset versus faults with moderate offset, with the latter being viewed as more likely to have ruptured to the ground surface, thus meriting a higher quality ranking. We chose to classify faults as having “moderate” offset if there was  $\geq 5$  cm of vertical separation, or if the correlation of units across the fault was uncertain due to textural changes, indicating that the lateral slip was reasonably large. Previous studies have documented rupture with up to 20 cm of vertical separation that terminated at different stratigraphic levels during the same prehistoric earthquake (e.g., Weldon et al., 2002; Bonilla and Lienkaemper, 1991). In other studies, earthquakes with displacement of only a few millimeters or less have ruptured to the ground surface (e.g., McGill and Rubin, 1999). Our selection of 5 cm to define “moderate” offset falls between these values.

Second, we adjusted the ranking to take into account the effects of uncertainties in stratigraphic correlation that made attribution of an indicator to a specific horizon challenging. Specifically, in cases where the upward termination of a fault was not distinct, and there were multiple horizons that could reasonably be associated with the upward termination, we assigned a quality ranking of 0. If the upward termination was indistinct or unclear, but there was an unfaulted unit that was distinguishable below the next higher earthquake horizon, we assigned a quality ranking of 1 for minor offset and 2 for moderate offset, because this was clearly an event distinct from the next younger event, even if the precise location of the earthquake horizon could not be determined. It is worth noting that our treatment of upward fault terminations was designed to produce a minimum number of paleoearthquakes. In other words, in cases where a fault terminated below the stratigraphic level of a known earthquake horizon elsewhere in the trench, and if there were no unfaulted layers precluding the fault from extending up to the earthquake horizon, we assumed that the fault did extend up to the previously recognized earthquake horizon.

Third, Scharer et al. (2017) made a distinction between folding and thickness changes that are “small” versus those that are “substantial,” with the latter being viewed as more likely to have resulted from coseismic deformation of the ground surface, thus meriting a higher quality ranking. We specified thickness changes of 20 cm or more to be “substantial,” thus justifying a ranking of 3 if a causative fault was not clearly identifiable or 4 if a causative fault was identifiable. Our selection of 20 cm reflected our subjective judgement based on observations in unfaulted portions of the trench where thickness changes and undulations in contacts smaller than this may have resulted from non-tectonic causes in some cases.

### Stratigraphic Correlation Rankings

Uncertainties in stratigraphic correlation at the 18th Avenue trench led to difficulty in tracing the event horizons along the trench and between the two

walls, thus producing additional uncertainty in the event recognition. Because of the broad width of the trench, only four distinctive layers could be confidently correlated between the east and west walls. Even along the same wall of the trench and in the absence of faulting, lateral facies changes, local channel scour, and areas of poor stratigraphy made it challenging to trace some stratigraphic units over long distances (>10 m). Most strata could be clearly correlated across faults with minor offset, but stratigraphic correlation was more difficult across a few of the faults with larger amounts of offset.

To address the uncertainty in our stratigraphic correlation of event indicators, we created a stratigraphic correlation ranking table (Table 4). This correlation ranking table required a “type locale” to be defined for each individual event. We selected the type locale from among the best-ranked event indicators for that specific event (i.e., where the event horizon could be narrowly assigned within a stratigraphic package) and located where it was possible to correlate layers at the type locale with other event indicators. The relative stratigraphic position of each event horizon was traced along the trench wall (i.e., within a particular stratigraphic package) from the type section to the other indicators that occurred at that stratigraphic level. A stratigraphic correlation rating between 1 and 5 was assigned based on the continuity of the package. A rating of 5 means an event indicator could be easily followed all the way to the type section, confirming it was located at the same stratigraphic level as the event horizon at the type section. A rating of 1 means that the correlation was uncertain enough to create ambiguity as to the event horizon to which this indicator should be associated. This situation could result from pinch out of marker beds, mismatch or changes in character of units across faults or along section, position of benches, or presence of bioturbated zones. It is worth noting that we attempted to assign each event indicator to an event that also had other indicators, rather than treating each indicator that had an uncertain correlation as a potential independent event. Our method, therefore, was biased toward producing the minimal number of events necessary to explain the observations.

### Characterizing the Likelihood of Each Event

We qualified the likelihood of a paleoearthquake at each stratigraphic horizon based on the quality and the number of individual event indicators. Following the example of Scharer et al. (2017), we used the terms “probable,” “likely,” and “very likely” to denote horizons with increasing probability of representing a paleoearthquake horizon. Also, like Scharer et al. (2017), we used the label “probable” when the number and quality of event indicators suggested at least a 50% likelihood of a surface-rupturing event at that horizon. At this site, we considered events that had three or more indicators with at least one having a quality rating of 2 or higher to be probable earthquakes. Those with one or two indicators with quality rankings of 3 or higher were considered likely or very likely, respectively (Table 5). Horizons with isolated, weak evidence that did not meet these criteria were not given an event number. As noted above, our treatment of upward fault terminations and our approach to correlating

TABLE 4. DESCRIPTION OF STRATIGRAPHIC CORRELATION RANKINGS

Quality	Description
1	Stratigraphic correlation of one or more event horizons is uncertain enough to create ambiguity as to the event with which this indicator should be associated.
2	The stratigraphic level of the indicator cannot be physically traced all the way to the type locale because it crosses one or more faults, benches or areas of poor stratigraphy, leading to a relatively high level of uncertainty, including the possibility that the indicator could correlate with an event other than the proposed event.
3	The stratigraphic level of the indicator cannot be physically traced all the way to the type locale because it crosses a fault, a bench, or an area of poor stratigraphy. The correlation of strata is somewhat uncertain, but correlation with the proposed event is much more likely than correlation with any other recognized event. This rating may be applied to an indicator on the opposite wall from the type locale for the event, as long as it is not far above or below one of the three layers that have been correlated between the walls (units E/W 290, E/W 610, or E/W 850).
4	The stratigraphic level of the indicator cannot be physically traced all the way to the type locale because it crosses a fault, a bench, or an area of poor stratigraphy, but the correlation of strata is fairly certain. This rating may also be applied to an indicator on the opposite wall from type locale for this event, as long as it is not far above or below one of the three layers that have been correlated between the walls (units E/W 290, E/W 610, or E/W 850).
5	The stratigraphic level of the indicator can be <b>physically traced</b> all the way to the type locale, with no uncertainty in correlation of strata across any faults located between the indicator and the type locale. This can only be true for indicators that are on the same wall as the type locale for event.

TABLE 5. CRITERIA FOR CHARACTERIZING THE LIKELIHOOD OF EVENTS

Likelihood	Description
Probable	Three or more individual event indicators with at least one having a quality ranking of 2. No indicator has a quality rank higher than 2.
Likely	At least one event indicator with a quality rank of 3 or higher. Must have 3–5 individual event indicators with at least a rank of 1.
Very likely	Two or more event indicators with a rank of 3 or higher.

earthquake indicators were both designed to produce the minimum number of events. It is quite possible that additional events occurred that were not identified due to these approaches. It is also possible that multiple events occurred at any of the identified horizons if no sedimentation occurred between events.

### ■ SITE STRATIGRAPHY

The orthorectified, georeferenced, and annotated photomosaics for the west and east walls of the trench are shown in Plate 1. A simplified representation

of the contacts and faults extracted from Plate 1 is shown in Figure 3. Within Plate 1, strata that could be traced were assigned unit numbers, with unit numbers increasing with stratigraphic depth.

Four correlatable units were used to anchor the stratigraphic numbering of units between the trench walls. The uppermost unit is unit 290, which is a 30-cm-thick silt layer with a distinct thin, brown clay at its base. This unit contains more charcoal fragments than any other unit within the trench. The next lower anchor unit is unit 610. On the east wall, this unit is distinguished by the presence of many large boulders (~0.5 m diameter) within a 0.5- to 1-m-thick layer of coarse sand with pebbles and granules. Boulders this large are not present within any other unit. On the west wall, this unit is sandier, and the boulders are smaller (~0.25 m), but it is still the coarsest unit on the west wall, and it is a similar depth below the surface. Immediately below unit 610, there is unit 620, which is composed of coarse sand, pebbles, and small boulders (~0.25 m diameter) on the west wall and pebbly gravel on the east wall. These two units are separated by a sharp contact. The lowest unit is unit 850, a muddy sand and gravel bed with a sharp upper contact. The unit is brownish in color compared to overlying units, which are grayer in color.

All units on the west wall have a "W" prefix before the unit number, and those on the east wall have an "E" prefix. Unit numbers between 0 and 99 were assigned to strata above the E1 horizon, numbers between 100 and 199 were assigned to strata between the E1 and E2 horizons, and so on. Except for units 290, 610, 620, and 850, it was impossible to correlate units between the two walls. Thus, units that have the same number but a different prefix (E vs. W) should not be interpreted as correlating at all across the trench, nor should units with a lower number on one wall necessarily be assumed to be younger than a unit with a higher number on the opposite wall. Uncertainties in correlation of the event horizons were addressed through the correlation ranking system described above (Table 4).

Some unit labels also include a suffix letter after the unit number. In regions where a layer could be traced or correlated with certainty, the suffix letter is the same. In cases where there was some uncertainty in the correlation of the layer across a fault, bench, or region of poor stratigraphy, a different suffix letter was used on each side of the feature interrupting the ability to continuously trace the layer. For example, unit W110A is a very fine sand layer that crosses a fault at meter 8 on tier 2 of the west wall (Plate 1). The plate shows a possible correlation of unit W110 across this fault, but because the correlation is not confirmed by other layers offset with a similar sense and amount, we call this unit W110B on the opposite side of this fault. Similarly, at meter 12 on tier 2 on the west wall, we make a proposed, but uncertain correlation of this unit across an area of poor stratigraphy, so the unit is labeled W110C.

### EARTHQUAKE HORIZONS

A complete listing and description of all evidence for each event, including event quality and stratigraphic correlation ratings, may be found in Table S1 in the Supplemental Material. Figure 4 summarizes these data by illustrating the number of indicators for each event, as well as their quality and stratigraphic correlation rankings. The following sections explain key pieces of event evidence in detail. When referring to event indicators, we abbreviate their location by providing the meter number followed by the wall on which the event indicator is located and the tier number in parentheses; e.g., m36W (tier 1) refers to tier 1 on the west wall at meter 36. As will be shown below, applying Table 5, we distinguished one very likely event (E1), four likely events, and three probable events.

**E1. Very Likely.** The most recent paleoearthquake at the 18th Avenue paleoseismic site has 16 event indicators. There are three pieces of evidence with a

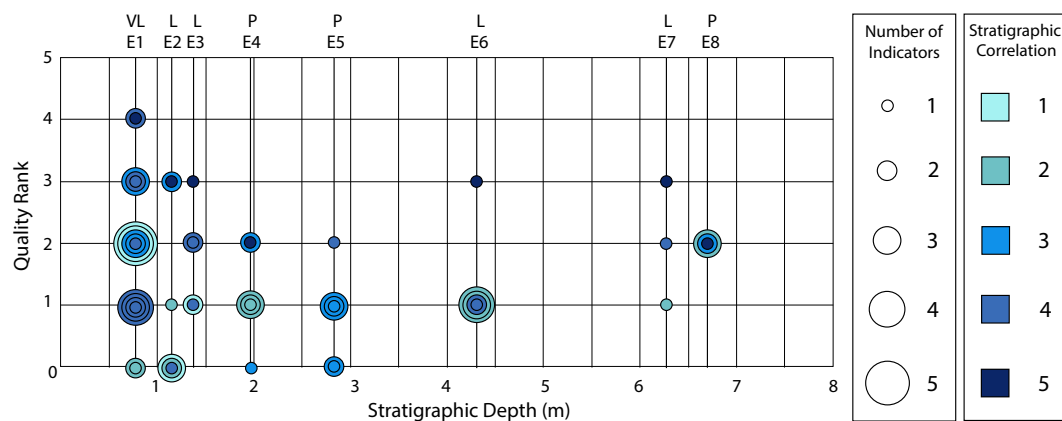


**Figure 4. Summary of event indicators.** Eight paleoearthquake horizons were identified in the 18th Avenue trench. Events are arranged according to stratigraphic depth on the horizontal axis. Vertical axis indicates quality ranking of each indicator, with higher numbers indicating better quality. The diameter of the symbol is scaled by the number of indicators in each rank. For example, earthquake horizon E1 has five individual event indicators with a rank of 2, producing a symbol diameter of 5. Color of symbols represents the stratigraphic correlation ranking of each event indicator. Indicators with a darker color can be correlated to the type section of the event with greater certainty. For example, of the five rank 2 event indicators for E1, one has a correlation strength of 4, two have a correlation strength of 3, and two have a correlation strength of 1. VL, L, and P indicate the event ranking of very likely, likely, and probable.

ranking of 3 and two with a ranking of 4 (Plate 1; Table S1), all of which involve sharp upward termination of faults with more than 5 cm of vertical separation and/or stratigraphic units that thin and pinch out against a scarp or folding horizon. An event indicator with a rank 3 is shown in Figure 5A. Two of these five strong pieces of evidence were on the west wall, and three were on the east wall. On each wall, the stratigraphic horizon associated with the strongest evidence for E1 could be traced with moderate to high certainty along the length of the trench. Although it was impossible to physically correlate

individual layers in this stratigraphic range between the two walls due to the configuration of the excavation, the sediment packages were similar on both walls (discontinuous 2- to 10-cm-thick layers of coarse sand with granules, fine sand, and silt). Given the similarity in the style of deformation and units both deformed by and postdating the deformation, we infer that the paleoearthquake closest to the present-day ground surface is the same on both walls. There were also 11 lower-rated indicators. Four were faults that terminated upward at the E1 horizon but that had very small amounts of vertical separation,

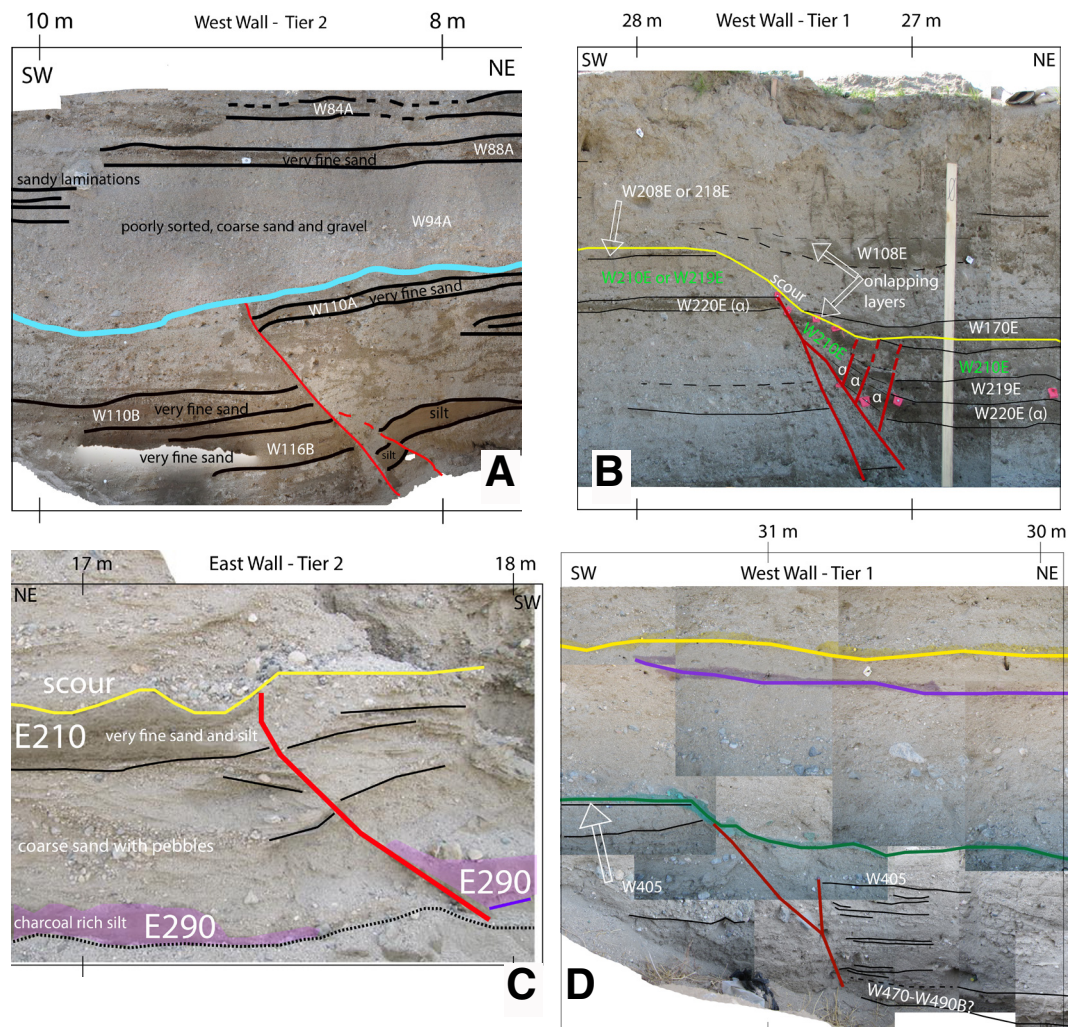


Figure 5. (A) Faulting evidence for event E1 at 8–10 m on tier 2 of the west wall. A fault terminates sharply at the base of an erosive contact (colored light blue). This fault displays at least moderate offset due to one of the following reasons: (1) There is a very fine sand layer that is visible on both sides of the fault and is labeled as W110A and W110B. If this layer is in fact the same layer, then there is at least 40 cm of vertical separation. (2) Alternatively, if layer W110A is not the same as layer W110B, then correlation of layers across the fault is difficult and suggests a large amount of lateral offset. A similar relationship is observed at this stratigraphic interval on the east wall. (B) Event 2 type locale at 26–28 m on tier 1 of the west wall. Series of faults terminate upward at the base of the yellow contact (E2 horizon). The nature of the yellow contact indicates that it is an erosional contact showing scour of the ground surface after deposition of W210E, followed by onlap of W170E and younger strata. This feature has a quality rank of 3. The labels “α” mark the locations of faulted pieces of layer W220E across the fault zone. (C) Exposures of an indicator for E2 on tier 2 of east wall. Here, mismatch of units across the fault indicates lateral separation when E210 was at (or below) the surface. The fault terminates at the base of an erosive contact (yellow line). This indicator has a quality rank of 3. Purple line shows E3 horizon for context. Dotted line delineates the base of the exposure and is not a geologic contact. (D) Type locale for event 4, at 30–32 m on tier 1 of the west wall. Lower part of figure includes photos from a hand-dug, deeper extension of tier 1 that are not included in Plate 1. Green line spray painted on trench wall (and drafted on the photomosaic) highlights the E4 horizon. A fault vertically separates layer W405 and is truncated by an erosional contact (green horizon) that marks the base of a sandy channel and the E4 horizon. The yellow and purple lines represent earthquake horizons E2 and E3, respectively.

and seven were faults that terminated 8–40 cm below the E1 horizon but that were assumed to have slipped during E1 because of the lack of any unfaulted stratigraphy that would preclude that interpretation (Table S1). It is possible that these seven faults that terminated 8–40 cm below the E1 horizon could represent one or more additional earthquakes between events 1 and 2, but we think it is more likely that they slipped during E1 and that the faults cannot be traced higher due to poor stratigraphy.

**E2. Likely.** There are six indicators for this event, including two with quality rank 3, one with rank 1, and three with rank 0 (Fig. 4). The type locale for this event has a quality ranking of 3 and is located at m28w (tier 1) (Fig. 5B). At that location, layer W220E is vertically separated ~40 cm across a zone of four faults. Layers W170E through W108E onlap across an erosive contact that appears to cap the faults. Alternate logging interpreted layer W170E as offset (correlating with W208E or W218E). While the stratigraphic units involved are not sufficiently distinct to determine which interpretation is correct, the event horizon in the alternate interpretation would definitely be below layer W108E, which thins and pinches out over the scarp. Given the location of samples that constrain the age of this event, the uncertainty in the exact paleo-ground surface does not impact the age estimate for the event. However, this uncertainty could allow for multiple events in the vicinity of the E2 horizon.

Another indicator for E2 is found at m17E (tier 2), where a fault terminates at the base of a gravel deposit (Fig. 5C). This fault has moderate vertical separation (12 cm), and layer E290 has been clearly offset. The fault can be traced to the base of a scour below which layer E210 is truncated by the fault. Layer E210 cannot be seen on the southwest side of the fault, suggesting at least moderate lateral offset. Because the earthquake horizon is represented by a scoured surface, it is possible that multiple events occurred at this horizon. This event indicator has a quality ranking of 3 but is on the opposite wall of the trench from the type locale, so we cannot say with certainty that these two indicators formed in the same earthquake. However, they are both located stratigraphically below E1 and above layer 290 (the base of which is the E3 horizon), which we consider to be correlated with certainty between the two walls, so this event indicator is given a stratigraphic correlation rank of 3.

Additional supporting evidence for E2 includes three event indicators that are found on the west wall (two with quality rank 1 and one with quality rank 0). At m7W (tier 3), there are distinct upward terminations of two faults with minor offset (rank 1). At m22W (tier 3), there are two faults with indistinct upward termini and minor offset (Plate 1). Both of these faults terminate at a stratigraphic level that is lower than E1, although the precise level of the event horizon is poorly constrained, and the fault cannot be traced downward to tier 2. Last, there is an event indicator with quality rank 0 that is found at m14E (tier 3). Here, there is a fault with moderate offset of layer E290 that stops at the bench level in between tiers 2 and 3. The exact location of the termination is unknown, but the termination lies stratigraphically above the event 3 horizon and below the event 1 horizon, suggesting it slipped during E2. The imprecise location of the E2 horizon at several indicators as well as uncertainty in correlations of indicators allow for the possibility for additional events between E1 and E3.

**E3. Likely.** There are six event indicators for E3, with ranks between 3 and 1. The strongest evidence for E3 (type locale) is the pinch out of a ≤40-cm-thick silt layer W290 on the west wall (between 8 and 20 m), centered within the main fault zone and underlying a ≤30-cm-thick package of laminated silty sand with gravel lenses. This ≤30-cm-thick package of laminated silty sand with gravel lenses thins to the north and south, and the underlying silt layer (W290) is absent from the remaining wedge-shaped section at meter 7 (Plate 1). We interpret this silt layer to have been deposited within a graben that formed during E3, resulting in a thick tabular layer of silt (W290) in the center of the graben and silty sand layers that later filled the depression and overlapped across the margins (layer W290 is at the base of the purple package in Fig. 3). Although the north end of the trench was not deep enough to reveal the faults that created this graben, it is clear on the west wall that a graben formed within the main fault zone (between 8 and 18 m) during E2. Thus, it is reasonable to infer that a graben may also have formed here during E3. Based on the stratigraphic evidence, we rank this event indicator with a quality rating of 3.

A similar charcoal-rich silt layer is also observed on the east wall at a similar stratigraphic level, so we correlate it with layer W290. On the east wall, layer E290 can be seen as far south as meter 20. Farther south, layer E290B is interpreted as a possible southward continuation of layer E290, but layer E290B is coarser and more poorly sorted than E290. We suspect that layer E290 thins and pinches out in the vicinity of meter 20, but this is obscured by the incision of a small gully into the trench wall that formed after excavation. Because of the uncertainty as to whether layer E290 pinches out near meter 20 or continues southward as layer E290B, we assign a quality rating of 1 for thickness changes in layer E290.

Three other event indicators associated with E3 are located on the east wall. First, at m18E and m19E (tier 3), there are two faults with significant lateral offset (indicated by the strong mismatch of layers across the faults) that are visible to the top of tier 3 but not visible in tier 2 (Plate 1). Layer E290 lies at the base of tier 2 and is unfaulted over the fault at 19 m, so this fault probably ruptured during E3, and we give this event indicator a quality ranking of 2. The event indicator at m18E (tier 3) has a quality ranking of 2 because layer E290 lies at the bench level and is not exposed over this fault at the base of tier 2. Last, at m27E (tier 2), a fault with minor displacement is capped by layer E290B, which is at the approximate stratigraphic level of layer E290 (and E3). We give this indicator a quality ranking of 1 because the fault has minor (<5 cm) displacement. The stratigraphic correlation ranking for this indicator is 1 (see Table S1). Overall, we rank E3 as *likely* because the evidence depends on our interpretation that the thickness changes in W290 at the type locale are a product of ground deformation, yet the potentially causative faults all extend higher than layer E290.

**E4. Probable.** There are six event indicators for E4, including two with rank 2, two with rank 1, and two with rank 0. The strongest evidence is found at m32W (tier 1) (type locale; Fig. 5D), where a fault produces moderate vertical separation of layer W405. This fault is truncated by an erosional contact (spray-painted green in Fig. 5D), which forms the base of a cobbly sand deposit

that is unfaulted. The quality ranking is only 2 because it is not clear if the units on the southwest side of the fault were eroded or if the deposit is conformable there. This potentially raises questions as to whether the scoured surface represents the same stratigraphic horizon on both sides of the fault, or whether the fault could have ruptured higher than this scour surface. In either case, there is at least one event at this scoured horizon.

At m23W (tier 2), there is a fault with ~6 cm of vertical separation (moderate offset) that is capped by layer W390, which appears to be unfaulted (Plate 1). The contact at the base of W390 is sharp directly above the fault, but it lacks clear continuity on both sides of the fault, so we assign a quality rating of 2 instead of 3. The event indicators at m32W (tier 1) and m23W (tier 2) are both on the west wall, but they are separated by ~9 m laterally and a bench. Our correlation of stratigraphic units suggests that these two indicators are at the same stratigraphic level. We assign a stratigraphic correlation rating of 3 to this indicator.

At m22W (tier 3), there is a fault with moderate offset of layer W555C. The fault could be capped by layer W470C, near the top of tier 3, or it could continue onto the base of tier 2, and be capped by W390C. In the latter interpretation, this fault would have slipped in E4. In the former interpretation, this fault would have slipped in an earthquake between events 4 and 5. Due to the significant uncertainty in the location of the upward termination of the fault, we assign it a quality ranking of 0.

At m32E and m36E (tier 2), there are two faults that terminate upward with minor vertical separation (quality ranking 1). We cannot be certain that these faults slipped in the same event as E4 on the west wall, but this would be the simplest interpretation and is compatible with the relative stratigraphic position of this feature. Last, at m24E (tier 3), there is a fault with minor offset originally mapped as being capped by unit E480, but it may extend upward and correlate with a fault in tier 2, which could be E3 or possibly even E4. Thus, it has a quality ranking of 1. Overall, E4 is considered a *probable* earthquake because all of the indicators are upward terminations with less than 10 cm of separation, and we do not observe stratigraphic evidence of significant vertical ground deformation (e.g., pinch out of units across grabens).

**E5. Probable.** There are six indicators for this event, including one with rank 3, three with rank 1, and two with rank 0. The best evidence and type locale can be found at m50W (tier 1), where we observe four faults with minor vertical separation of layer W590D that are all capped by the unfaulted layer W490D (Fig. 6A). Total vertical separation across the zone is ~10 cm. Therefore, we assign this moderate offset rank 3. The faults may terminate at or up to 20 cm below layer W490D. The 20 cm interval within which the earthquake horizon lies is bracketed by radiocarbon samples A18 and A24, as well as by luminescence samples L13 and L07. Because there are no dated samples from within this 20 cm interval, the uncertainty in the exact event horizon does not affect the event age.

At m26E (tier 3), three faults with minor offset downdrop a debris-flow deposit (E520) into a small graben that is capped by the unfaulted clayey silt layer E490 (Fig. 6B). We give each of these faults a quality ranking of 1. At m23E

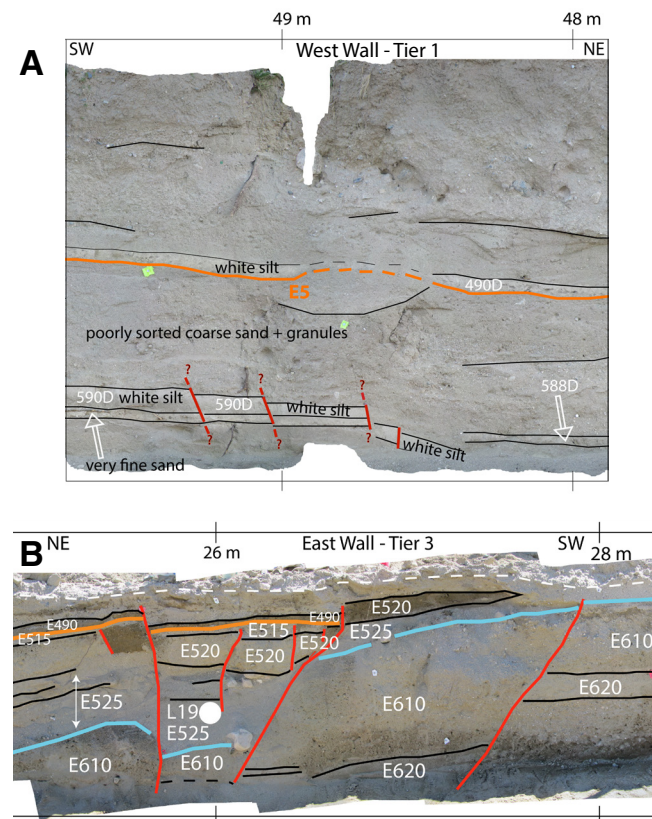


**Figure 6.** (A) Type locale for event 5, at 48–50 m on tier 1 of the west wall. Four faults (red lines) offset unit 590D but do not appear to offset unit 490D above. The top of the image is the ground surface. (B) Indicators for events 5 and 6 (orange and blue lines, respectively) at 21–27 m on tier 3 of the east wall. Several minor faults slipped in E5 and are capped by an unfaulted layer E490. (Southwest of the fault at meter 27, the event 5 horizon is faulted up into tier 2.) Event 6 is illuminated by layers E520 and E525, which triple in thickness to the northeast (left), suggesting they were deposited within a depression that formed when E610 was at the ground surface. White dashed line marks top of tier 3. White circle represents location of luminescence sample L19.

(tier 3), we also observe a fracture in layer E520 that may connect downward to a fault (quality rank 0) (Fig. 6B). These indicators from the east wall are all clearly capped by the same horizon (E490). At m32E (tier 2), there is a fault splay with unknown but likely very minor offset that is capped by layer E440, assigned a quality ranking of 0. Because E490 pinches out before reaching this location, E440 likely represents the first sediment deposited after E5, and this fault splay likely slipped in E5. Correlation of evidence for E5 between the two

walls is uncertain, but this represents the simplest interpretation. We qualify E5 as probable because all of the event indicators are upward terminations, and no unit thickness changes can be clearly followed above the terminations.

**E6. Likely.** There are five indicators for E6. There is one event indicator with a rank of 3 and four additional event indicators with a rank of 1. The type locale is located at m22–27E (tier 3). Here, the thickness of layers E520 and E525 decreases from 60 cm at 23 m down to 20 cm at 26 m (Fig. 6B). We interpret these layers as part of a postearthquake depositional sequence that filled a closed depression that was formed during E6, similar in character to basin formation in the youngest events. The large and rapid changes in unit thicknesses indicate filling of a depression, so we give it a quality ranking of 3. The earthquake horizon is interpreted to be at the top of layer E610, which is a thick, bouldery debris-flow deposit that has no noticeable thickness change across this region of the trench.

On the west wall, unit W610 consists of boulders within moderately well-sorted coarse sand. We interpret this layer to be the continuation of debris-flow deposit E610, on the opposite wall of the trench. At m23W (tier 4), two faults produce minor vertical separation within layer W610 and are capped by unfaulted layer W590 (Plate 1), and they are given a quality ranking of 1. Farther south on the west wall, we tentatively correlate the thick clay layer W590 with silt layers W590B, W590C, and W590D, which is the most laterally continuous silt layer to the south. At m38W and m39W (tier 2), we observe two faults that have produced minor vertical separation (~2 cm) of layer W604C and are

capped by unfaulted sorted layer W590C. If our correlation of layer W590 with W590C is correct, then these two faults provide additional indicators (quality rank 1) for E6. However, it is also possible that layer W590 at 23 m correlates with layer W604C (at 36–50 m). If this alternate correlation is correct, then the two minor faults at 38 and 39 m would be indicators for an event between events 5 and 6.

**E7. Likely.** There are three event indicators for E7, one with rank 3, one with rank 2, and one with rank 1. The strongest evidence can be seen at the type locale at m32E (tier 4). Here, we observe an 80-cm-thick package of very fine sand, silt, and clay (E670–E690) that thins to 10–15 cm (E690) as it approaches a fault at m34E (Fig. 7); we give a quality rank of 3 due to the substantial thickness change observed here. The causative fault (at 34–36 m) has reruptured in a younger earthquake.

The quality rank 2 indicator can be seen at m36E (tier 3) (Fig. 7). Here, we observe a fault with 5 cm of vertical separation in the upper part of tier 4 (pebble layer E710), capped by an unfaulted fine sand layer (E690) at the base of tier 3. Because the fault and the capping layer are not visible on the same tier, this event indicator is given a quality ranking of 2 instead of 3. Correlation of units between 32 and 36 m on the east wall is clear enough that we are confident that these two indicators represent the same earthquake horizon. The indicator at m36E (tier 3) has thus been assigned a stratigraphic correlation ranking of 4 with respect to the type locale at 32 m.

The rank 1 indicator can be seen at m28W (tier 4), where layer W690 thins to the south and pinches out (Plate 1). The causative fault is likely the fault at

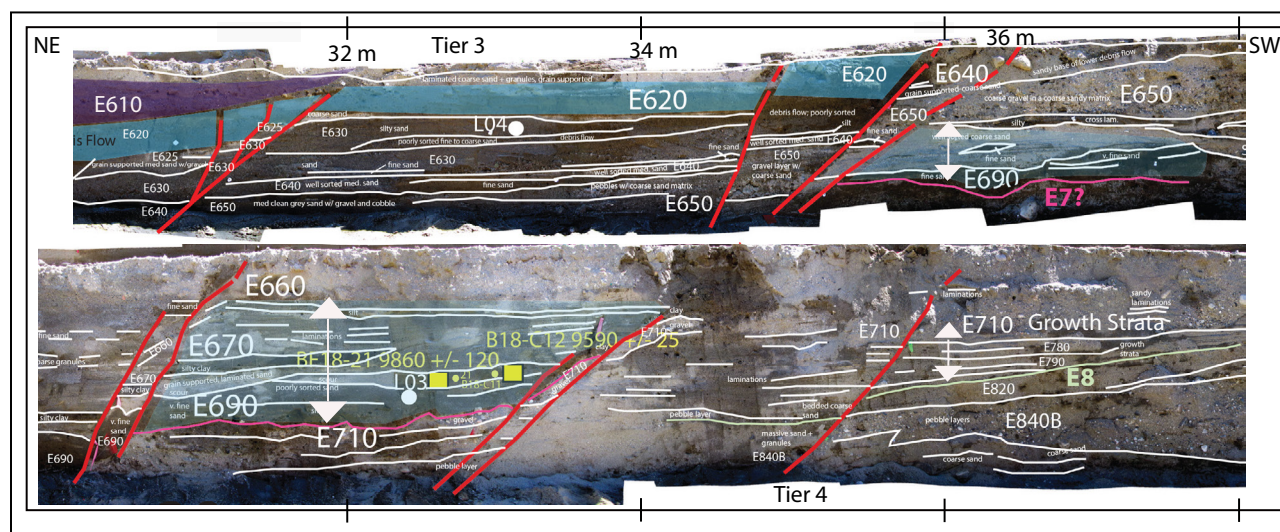


**Figure 7.** Event 7 and 8 evidence showing type locale for event 7 at 34 m on tiers 3 and 4 of the east wall. Layers E670–E690 (shaded pale blue) thin to the southwest as they approach the fault at m34E. An indicator for event 8 at 36 m on tier 4 is shown in the lower photomosaic. Layers E780–E790 thin to the south, filling a depression formed when layer E820 was tilted during event 8.

28 m. Although we observe moderate thickness change, which suggests filling of a closed depression, layer W690 is only exposed over a short distance (~2 m), so the full extent of the closed depression is not visible. Therefore, we assign a quality ranking of 1. It is not clear whether layer W690 is the same as layer E690 on the opposite wall of the trench, but it is clear that on both the east and west walls, there is evidence for two events (events E7 and E8) between layers 610 and 850, both of which can be correlated between the two walls of the trench with a high degree of confidence.

Overall, E7 is considered *likely* because the mismatch of unit thickness at the type locale (Fig. 7) occurs across a fault and may be the product of later lateral motion (the fault strand extends almost to the surface and last ruptured in E1) rather than local graben formation and filling.

**E8. Probable.** There are three event indicators (all rank 2) for the oldest event horizon observed at this paleoseismic trench site. Two event indicators with a quality rank of 2 are located at m31W and m36W (tier 4), with the latter being the type locale. At m31W, there is a fault with moderate vertical separation (22 cm) of layer W815-W815B, which is then capped by a layer of fine sand (layer W790) (Plate 1). The basal contact of layer W790 is sharp directly above the fault, but it lacks clear definition to the north; therefore, we assign a quality rating of 2 rather than 3. At the 36 m location (type locale), we observe a fine sand layer (W790C) that thins to the south and pinches out against a fault at 36 m. We infer that layer W790 filled a depression that formed during E8. Only a small section of the pinching layer W790 is visible just below bench level. Therefore, we assign a quality ranking of 2 rather than 3. We tentatively correlate layer W790 with W790B and W790C, which would imply that these two event indicators were caused by the same event. However, it is possible that W790B correlates with W815B instead of with W790, and that W790 has no correlative unit south of the fault strand at 32 m, so we assign a correlation ranking of 3. In addition, it is not clear whether layer W790 is the same as layer E790 on the opposite wall of the trench. Nonetheless, it is clear that on both the east and west walls, there is evidence for two events (events 7 and 8) below layer 610 and above layer 850, and both units 610 and 850 can be correlated between the two walls of the trench with a relatively high degree of confidence.

At m36E (tier 4), layers E780 and E790 thin and pinch out to the south, and we infer these layers represent growth strata filling in a depression produced by an earthquake (Fig. 7). Movement on the fault at 38 m may have caused the depression in which these growth strata were deposited. Although the thickness changes are moderate, the fault at 38 m is not clearly linked to the growth strata, leading to quality rank of 2 for this event indicator.

## PALEOEARTHQUAKE AGES

### Radiocarbon and Luminescence Dating

Layer ages were obtained from 34 radiocarbon-dated detrital charcoal samples and 17 sediment samples dated using post-IR IRSL techniques (Tables 1

and 2). All dates are plotted in Figure 8 as a function of stratigraphic depth measured at m24W down to layer W620, and then at m34 for layers older than W620 (Fig. 3). These sections were selected because they are within a wide, fault-bounded block with clear stratigraphy and are close to the area where layers are thickest. On Figure 8, all samples from the east wall, and samples from the west wall that are not from the type section are shown with vertical error bars that indicate the uncertainties in the stratigraphic positions of these samples relative to the type section.

The stratigraphic thickness of 9 m exposed in the trench was deposited within the past ~7000 yr, indicating an average depositional rate of ~0.13 cm/yr. Based on the youngest samples at each depth, the sedimentation rate appears to have been relatively constant across the section, yet it could have been variable from unit to unit given the relatively sparse dating. The longest possible depositional hiatus can be no more than the 1–1.5 k.y. interval between samples L01 and L17 (~4–5 m depth). There is no clear indication of a hiatus at this time, and a hiatus this long is only possible if deposition stopped immediately after the layer containing L17 formed, and the overlying 1 m of sediment between sample L01 and L17 was deposited very rapidly. Based on texture and bedding, the layers between these two samples could have been deposited in a few depositional events. Episodes of rapid sedimentation may have also occurred, such as between samples L17/L18 and L20/L04/L02, which all have nearly the same age within the 1 $\sigma$  uncertainties, despite spanning ~1.5 m of stratigraphic depth. This depth range is dominated by the two thickest units in the trench, the boulder units 610 and 620, which were likely deposited very rapidly, potentially during the course of one or a few storms. The presence of scouring within some areas (e.g., Figs. 5A, 5B, and 5C) suggests that parts of the record are locally missing.

### Paleoearthquake Model Ages

We used OxCal (Bronk Ramsey, 2009) to estimate the earthquake ages. OxCal uses Bayesian statistics to model posterior ages for paleoearthquakes based on all chronological constraints such as relative stratigraphic position and layer groups. Dates from the same layer, or from layers that we infer correlate with each other, were modeled using the “Phase” command such that relative stratigraphic position within the layer group was not applied (Bronk Ramsey, 2009).

The range of ages for several intervals shown in Figure 8 presents a challenge for constructing a straightforward age model. For example, samples A44 and C10 at 2 m stratigraphic depth have ages that differ by 2000 yr, as do samples A18 and A39 at 2.75 m stratigraphic depth. Many studies have shown that it is common for detrital charcoal samples to be older than the age of the layer from which they were collected by an amount that depends on the length of time between when the plant material stopped growing and when the sample was deposited in the location from which it was collected (e.g., Philibosian et al., 2011; McGill et al., 2002; Fumal et al., 2002). Aside from



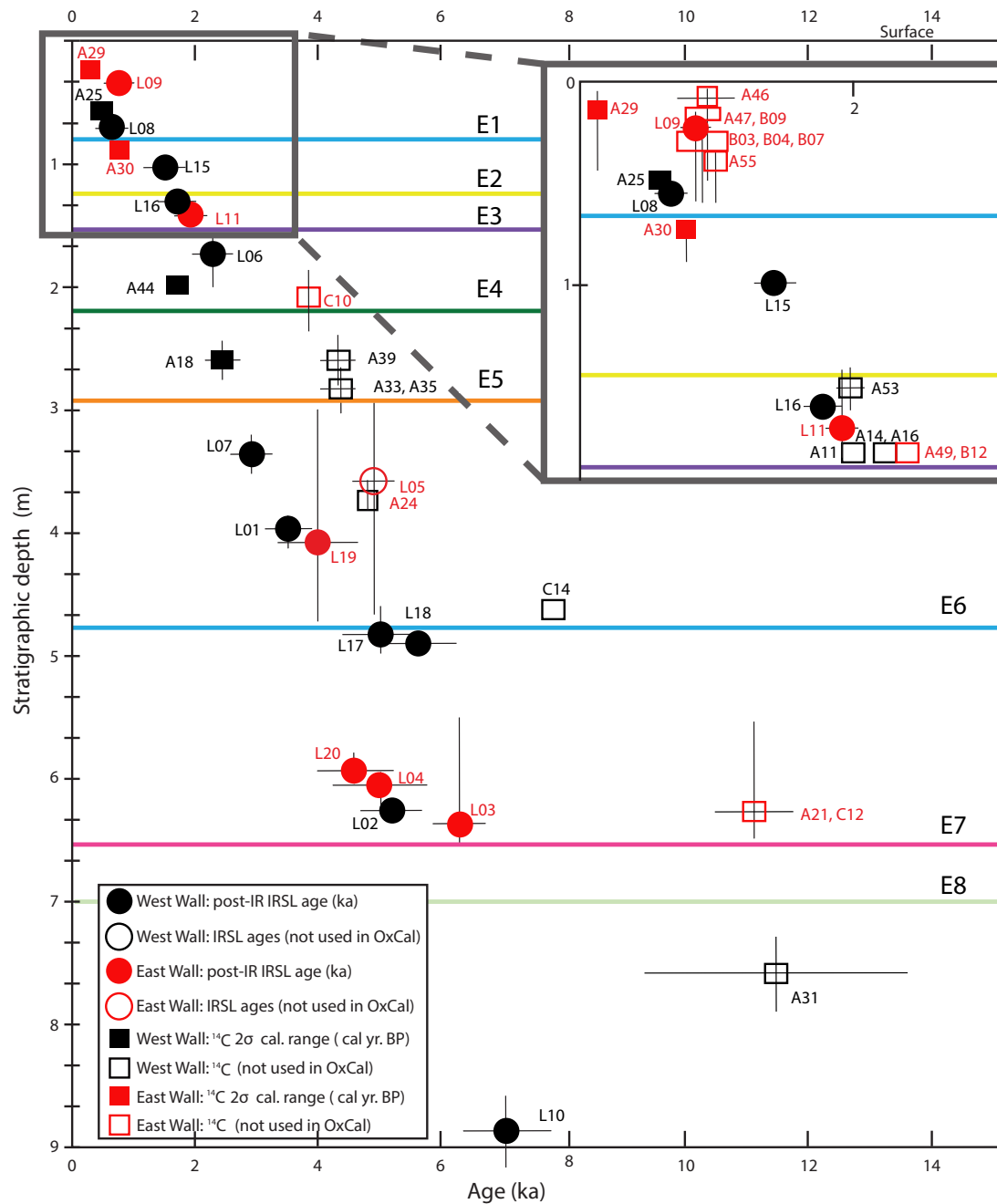


Figure 8. Calibrated radiocarbon and post-IR IRSL ages as a function of stratigraphic depth. Stratigraphic depth was measured on the west wall at 24 m from the surface to the base of unit 620 (see Plate 1) and at 34 m from the base of layer 620 to the base of the trench. Vertical error bars show uncertainties in correlating sample locations from the east wall or from other fault blocks on the west wall with the type section. Solid symbols show ages that were included in our preferred OxCal model; open symbols show samples excluded from that model. Inset shows all ages from the upper 1.6 m.

contamination of the sample, the only way for charcoal to underestimate the depositional age of a layer is if it was a root or was brought into the section by bioturbation. We were careful in the field to avoid collecting roots or any charcoal samples from obvious filled burrows or areas lacking clear stratigraphy, which could potentially be bioturbated zones, and we reviewed photographs of the sample locations to evaluate the potential for unrecognized bioturbation at each sample location. To construct our preferred age model, we therefore omitted any charcoal samples with dates that were older than other charcoal or luminescence samples from the same layer or lower layers. In Figure 8, dated samples that were included in our preferred age model are plotted with filled symbols, and those that were excluded are plotted with open symbols.

In total, 29 out of 34 radiocarbon dates were omitted from our preferred age model, which thus relied heavily on the IRSL ages to constrain the timing of past earthquakes. The omission of this many radiocarbon samples is supported by previous studies that have shown wide ranges of radiocarbon ages for charcoal samples from the same layer (e.g., McGill et al., 2002; Fumal et al., 2002; Philibosian et al., 2011). In the 18th Avenue trench, we also collected multiple samples from the same depths that have mean radiocarbon ages separated by as much as 2000 yr (e.g., samples A44 and C10 at ~2 m depth and A18 and A39 at ~2.6 m depth), suggesting that detrital lag times can be at least 2000 yr long on the Mission Creek fan. Fumal et al. (2002) also found lag times of up to ~600–1000 yr for charcoal samples from the same layer at a site on the Mission Creek strand at the Thousand Palms site, located ~20 km to the east, and that site, like the 18th Avenue trench, also has a large source catchment.

One IRSL sample from the east wall (L05) was also excluded from our preferred age model because it was older than most other samples at that stratigraphic depth, and it had large uncertainty in its stratigraphic depth relative to the type section on the west wall. The results of the preferred OxCal model are shown in Figure 9 and Table 6.

While it is common practice in paleoseismic studies to omit charcoal samples that are older than other charcoal samples from the same or underlying layers (McGill et al., 2002; Fumal et al., 2002; Philibosian et al., 2011), a factor that may be of concern in this study is that we also omitted charcoal samples that were older than luminescence samples from the same or underlying layers, resulting in an almost exclusive reliance on the IRSL ages. Therefore, we also created an alternate model that took a different approach based on the observation that the 2000 yr lag was based on only two radiocarbon samples. In contrast to the preferred model, the alternate model (Fig. A1) starts with the assumptions that those samples (A44 and A18) were contaminated by younger material (which can occur during sample collection and preparation), and that radiocarbon samples C10 and A39 were accurate. Samples A44 and A18 were thus removed from the OxCal model, along with sample A31, because it was much older than the five IRSL samples near the base of the section, which we assume are correct based on their reproducibility. To achieve an OxCal agreement index >50%, samples L16, L06, L07, and L01 were also removed because they were notably younger than both radiocarbon and IRSL samples

in the same phase. Given that the IRSL signal measured for these samples is observed not to fade through time (Fig. A2), the only reasonable explanation for an apparent IRSL age that is too young is postdepositional mixing. Considering that it is unlikely that postdepositional mixing of grains would systematically shift ages in a way that is stratigraphically consistent, these were not removed in the preferred model. However, this alternative model has some advantage of retaining more of the original radiocarbon data, as it used 20 of the original 34 radiocarbon and 13 of 17 IRSL samples. In comparison to the preferred model, this approach produced much older earthquake ages for E2–E6 (Fig. 10; Table 6). Although both models are feasible, we chose the preferred model because it is common for detrital carbon samples to be older than true depositional ages, and the fading tests (Fig. A2) indicated that the IRSL samples are unlikely to be biased too young.

## DISCUSSION

### Recurrence Intervals

As shown in Figure 4, the overall number of observations and quality rank of event indicators decrease with depth. There are several reasons why the evidence for older events is weaker than that for the younger events. First, the older strata are only exposed within a small portion of the fault zone. Second, evidence for older events has been overprinted by younger earthquakes, making interpretation more difficult. Stratigraphic correlation of event indicators to their respective type locales was also a major challenge in this trench at all stratigraphic levels, but it was compounded for older events due to increased difficulty in correlating layers across faults in which the cumulative lateral offset in multiple events was large.

The earthquake record at the site includes evidence for five events in the upper 3 m, which occurred in the past 2.4–3.3 k.y. (age range for E5). The mean recurrence interval for these five events on the Banning strand is 490 yr (95% range 390–600 yr). The individual intervals between each of these five events are very similar to the mean (Fig. 10). As noted above, we cannot rule out the possibility that additional earthquakes may have occurred and not been recognized. If the alternate age model is correct, ages for E2 through E6 are 600–1800 yr older than in the preferred model, producing a mean recurrence interval of 940 yr, i.e., nearly twice as long as that in the preferred model (Fig. 10).

Only three events are recognized in the lower 6 m, during a 2.4–4.7 k.y. period between events E5 and E8 (Table 6). This suggests that either we are missing events in the lower section, or the recurrence pattern at the 18th Avenue site is variable. We cannot rule out either possibility. However, it is likely that the older part of the earthquake record at this site is incomplete due to limited exposure in which to make observations of the older stratigraphy. Specifically, the trench does not expose stratigraphy older than E3 north of m16, nor does it expose stratigraphy older than E5 north of m20. Faults with large

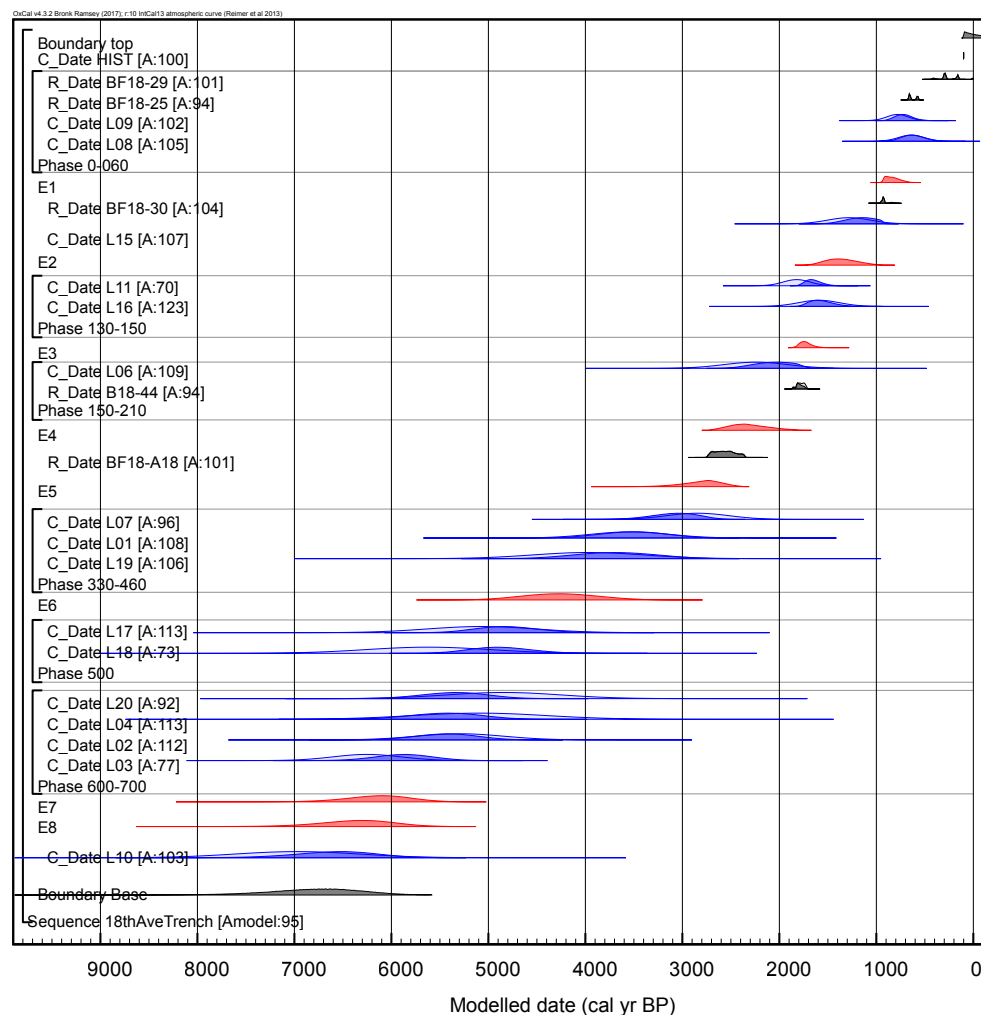


Figure 9. OxCal model used to estimate earthquake ages. Ages are plotted as a function of stratigraphic position; blue shapes are post-infrared infrared stimulated luminescence (IRSL) ages, gray shapes are radiocarbon ages, and red shapes are resultant earthquake ages. Brackets indicate samples from same phase (samples from same layer or from layers for which relative stratigraphic position cannot be differentiated). In the Bayesian approach used within OxCal, the ages of samples above and below a given sample are used to reweight the probability density function for that sample so as to yield a set of ages that are stratigraphically consistent with each other as well as being consistent with the a priori (measured) ages of each sample. Pale color shows prior probability density functions (PDFs) obtained for the ages of individual samples. Opaque colors are the posterior PDFs for each sample. This model assumes that charcoal samples provide a maximum age. The model also assumes that IRSL minimum age model methods have correctly estimated the depositional age of the sediment. To achieve an agreement index of >60% (Lienkaemper and Bronk Ramsey, 2009), 29 radiocarbon samples that were older than stratigraphically lower IRSL or radiocarbon samples were removed. An alternate model that retained more radiocarbon ages is provided in the Appendix (Figs. A1 and A2).

vertical separations are present in the trench north of m20, yet we had no way to investigate paleoearthquakes older than E5 on these faults. In addition, if there was a 1–1.5-k.y.-long hiatus between the deposition of samples L17 and L01, as permitted in the dating, it is possible that we missed the detection of events during this period.

If the full record of up to eight earthquakes is complete, the average recurrence interval during the past ~7000 yr would be ~790 yr (95% range 680–910 yr; Table 7). If the alternate age model is correct, the average recurrence interval for all eight events would be 770 yr (95% range 680–870 yr; Table 7).

### Comparison to Other Paleoseismic Sites

The mean recurrence interval between the past five surface-rupturing earthquakes at the 18th Avenue site is 490 yr (95% range 390–600 yr), which is longer than it is for the three sites on the Coachella section and Mission Creek strand (116–300 yr; Philiposian et al., 2011; Sieh and Williams, 1990; Fumal et al., 2002) and shorter than or overlaps with the measured recurrence intervals at the Cabazon trench site on the San Gorgonio Pass fault zone (two intervals between three paleoseismic events have been identified: ~450 and ~1600 yr;

TABLE 6. EARTHQUAKE AGES AT 18TH AVENUE PALEOSEISMIC SITE

	Preferred model (calibrated yr B.P.)			Alternate model (calibrated yr B.P.)		
	Mean	95% range		Mean	95% range	
E1	830	945	690	830	945	690
E2	1360	1650	1050	1985	2085	1900
E3	1730	1850	1590	3325	3865	2760
E4	2315	2665	1930	3920	3965	3880
E5	2805	3225	2430	4595	4815	4425
E6	4260	5000	3505	5080	5360	4860
E7	6150	6840	5490	6080	6675	5510
E8	6375	7175	5620	6245	6930	5595

Wolff, 2018; Scharer and Yule, 2020). Thus, earthquakes at the 18th Avenue site on the Banning strand occur less frequently than those on the Coachella section and Mission Creek strand but more frequently than those on the San Gorgonio Pass fault zone.

Figure 11 shows the ages of paleoearthquakes at the 18th Avenue site in comparison with prehistoric earthquakes at other sites on the southernmost San Andreas fault. One of the most interesting features shown in Figure 11 is that the age of the two most recent paleoearthquakes at the Cabazon site and 18th Avenue site are contemporaneous. To illustrate how such observations can be modeled as ruptures, we provide two possible rupture histories for the southernmost San Andreas fault near San Gorgonio Pass (Figs. 11B and 11C). Both models are consistent with the dates of paleoearthquakes on the southern San Andreas fault, but they show different correlations that could reflect different geometric segmentation; many other scenarios are possible given the input data (Scharer and Yule, 2020). The first scenario (Fig. 11B) shows an event ca. 1200 CE that connects contemporaneous earthquake ages at Millard Canyon (Mi1), Cabazon (Ca1), and 18th Avenue (E1). Because no earthquakes at Burro Flats (Bu) or Coachella (Co) overlap in age with the limits of Ca1 and E1, this rupture was confined to the San Gorgonio Pass fault zone and Banning strand. This is also consistent with no rupture observed in the past 600 yr at the East Whitewater site on the Garnet Hill strand (Cardona, 2016). The second scenario shows an alternative that separates this rupture into two earthquakes between ca. 1100 and 1300 CE. In Figure 11C, E1 and Co5 are connected for a rupture along the Banning strand and Coachella section, followed by a rupture that is centered in San Gorgonio Pass fault zone, connecting Mi1 and Ca1. Although the San Gorgonio Pass fault zone rupture is relatively short, it could have continued onto other mapped faults in the region; for example, the San Gorgonio Pass fault zone extends for another 40 km to the west (Fig. 11; Yule and Sieh, 2003).

In contrast to the more segmented ruptures ca. 1200 CE, it is possible that the entire model domain in Figure 11 ruptured at 600 CE, as ages permit a San Bernardino–San Gorgonio Pass fault zone–Banning–Coachella rupture, potentially similar to the “Shakeout scenario” (Jones et al. 2008). Scharer and Yule

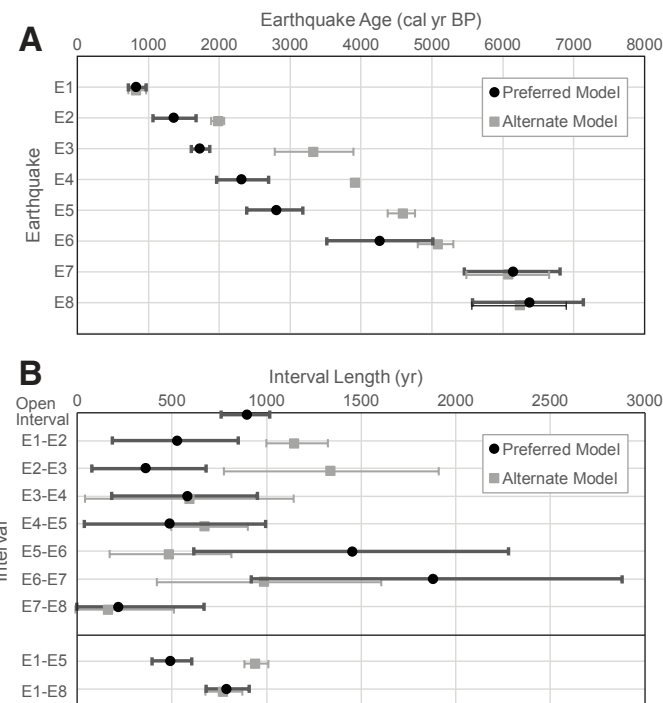


Figure 10. Comparison of preferred and alternate earthquake ages (A) and intervals (B). The preferred model omits 29 of the radiocarbon ages, assuming they reflect significant inheritance due to long transport times. It also assumes that the minimum age model accurately resolved the depositional age of the infrared stimulated luminescence (IRSL) samples. The alternate model (Fig. A1) omits five radiocarbon samples, assuming they were affected by young contamination. The alternate model retains more ages overall and produces older ages for E2 through E5.

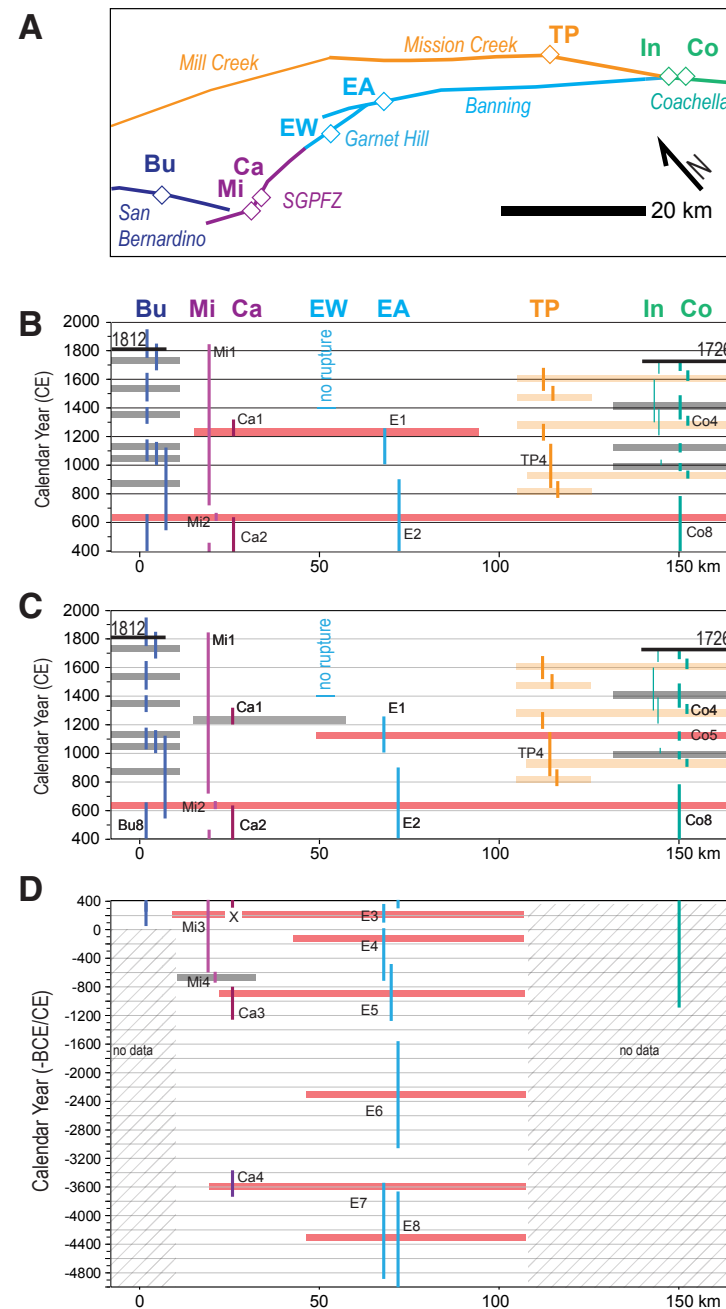
TABLE 7. EARTHQUAKE INTERVALS AT 18TH AVENUE PALEOSEISMIC SITE

	Preferred model (yr)			Alternate model (yr)		
	Mean	95% range (calibrated yr B.P.)		Mean	95% range (calibrated yr B.P.)	
Open interval	900	1015	760	830	945	690
E1–E2	530	185	850	1150	1000	1325
E2–E3	365	75	680	1340	775	1910
E3–E4	585	180	950	595	40	1145
E4–E5	490	35	995	675	495	900
E5–E6	1455	615	2280	485	170	815
E6–E7	1885	920	2880	990	420	1605
E7–E8	220	–5	670	165	–10	510
E1–E5	493	393	605	941	884	1010
E1–E8	791	680	909	771	678	872

**Figure 11.** (A) Map showing paleoseismic sites along the southernmost section of the San Andreas fault in the Coachella Valley and San Gorgonio Pass region. Site abbreviations and references are as in Figure 1. SGPFZ—San Gorgonio Pass fault zone. (B–C) Example paleoseismic rupture histories for this region during the past 1600 yr. Vertical bars are earthquake ages from each site (95% range), where select events are labeled with their site abbreviations followed by the event number (e.g., Mi1 is event 1 at Millard Canyon). Events from the 18th Avenue site are labeled E1, E2, etc. Horizontal bars are possible ruptures that are consistent with the ages. Black lines represent historic 1812 (Topozada et al., 2002) and early historic ca. 1726 (Rockwell et al., 2018) ruptures. Red ruptures connect events at 18th Avenue on the Banning strand with other sections of fault; orange ruptures connect Mission Creek strand to Coachella section but do not rupture the Banning strand at the 18th Avenue site. Gray horizontal bars mark ruptures restricted to a single section within the scope of this diagram. Ends of ruptures are schematic, generally guided by location of geometric complexity (e.g., splay, bend). Age ranges for the ruptures are not shown but can be wide given the ages of the contributing sites (see Scharer and Yule, 2020). (D) Rupture history for older section (note change in scale). Only the Cabazon site extends as long as the 18th Avenue site but has only four known events in that period.

(2020) showed that this rupture had the potential to extend onto the Mojave section of the San Andreas fault. As shown here, this single through-going rupture at 600 CE would have been at least 150 km long, equivalent to M 7.5 or greater using regression equations in Wesnousky (2008). It is worth noting that the event at 600 CE could also be modeled as separate ruptures. Only the two most recent paleoearthquakes at the 18th Avenue site occurred within the time period represented by the Burro Flats record. Although the most recent event at the 18th Avenue site may correlate with Mi1 and Ca1 on the San Gorgonio Pass fault zone, there is no record of an earthquake at this time on the San Bernardino strand at Burro Flats. The 600 CE event is the only Banning strand event that could potentially correlate with an earthquake on the San Bernardino strand within the past 1600 yr, assuming all the paleoseismic records are complete.

A general observation is that in the past 1600 yr, there have been eight earthquakes each at the Burro Flats (San Bernardino strand) and Coachella (Coachella section) paleoseismic sites, while there have only been two at the 18th Avenue site on the Banning strand and at the Cabazon site on the San Gorgonio Pass fault zone, and five on the Mission Creek strand at Thousand Palms. The more frequent earthquakes outside of the sites along the Banning strand and the San Gorgonio Pass fault zone contrast with the fewer earthquakes at those locations and control potential rupture histories in the area. Interestingly, a maximum of two earthquakes connecting the Coachella and northern Banning strands is permitted in the past 1600 yr. This requires that six ruptures on the Coachella section either terminated on the southern Banning strand, extended onto the Mission Creek strand, or ended at the splay (see also Scharer and Yule, 2020). These data generally support the dynamic rupture models of Douilly et al. (2020), which found that rupture on the Banning strand was less likely to occur given the geometry of the fault splay. Only the most recent earthquake at the 18th Avenue site occurred during the period observed at the Thousand Palms site on the Mission Creek strand, and it may have occurred at the same time as TP4 (Figs. 11B and 11C), allowing the



possibility of rupture jumping from the Mission Creek to the Banning strand, as seen in some dynamic rupture model configurations (Douilly et al., 2020).

Prior to 400 CE, paleoearthquake data from nearby sites are sparse (Fig. 11D); only the Cabazon site has a record as long as the 18th Avenue site (Fig. 11D). In this time period, two ruptures connecting 18th Avenue and Cabazon are permitted, ca. 3600 BCE and 1000 BCE. While the E3 and Mi3 ruptures were contemporaneous, there is no correlative event at Cabazon if Ca2 ruptured with Mi2, as indicated. Wolff (2018) noted that missing events were likely at Cabazon, which is shown with an X on the speculative rupture ca. 200 CE that would span the Banning and San Gorgonio Pass fault zone.

### Implications for Average Slip per Earthquake

The Banning strand of the San Andreas fault has a Holocene slip rate of 2.3–6.2 mm/yr (Gold et al., 2015), based on a fan offset at the Painted Hills site, ~8 km northwest of the 18th Avenue site (Fig. 1). Given the elapsed time since the most recent event (945–690 calibrated years B.P. or cal yr B.P.) and the slip rate at Painted Hill, we calculated that the fault could produce slip of 1.6–5.9 m in the next earthquake, using a slip-predictable model, and assuming a relatively constant strain release. Using the average recurrence interval of 390–610 yr between events E1 and E5 and the slip rate, we estimated that the average slip in these past five events was 1–4 m. These estimates of average slip per earthquake are simple because they do not include uncertainties related to variability in strain release, and they assume on-fault displacement is comparable at each location. Alternatively, as the fan age at Painted Hill overlaps with the section dated at 18th Avenue, we can infer that the fan has experienced 6–8 earthquakes if all the ruptures spanned the distance between both sites. This would produce an average slip per event of 2.5–5 m for the northern Banning strand, assuming the 18th Avenue site record is complete. We note that this range is similar to that predicted from the accrued slip since the most recent event, which may indicate the trench record is complete, or nearly so.

### CONCLUSIONS

The 18th Avenue site provides the first dated paleoseismic record constructed on the Banning strand of the southernmost section of the San Andreas fault. This 7000-yr-long record can now be compared to paleoseismic records on the neighboring strands that make up the complex network of faults in the southern section of the San Andreas fault. Eight horizons contained evidence of paleoearthquakes based on sedimentological responses to deformation and fault terminations at or below each horizon. These earthquakes were qualified based on the record of deformation and our ability to correlate across this wide trench; E1 is considered very likely; E2, E3, E6, and E7 are considered likely; and E4, E5, and E8 are considered probable. Based on the stratigraphy, dating uncertainties, and physical limits of the trench exposure, the likelihood

of missed events is greatest in the older parts of the section, below E5. The most recent event occurred 945–690 cal yr B.P. The open interval is longer than the average interval between events E1–E5 (390–600 yr), but it is shorter than the interval between events E5 and E6 and between events E6 and E7. The longer average interval for the entire section (680–910 yr for events E1–E8) may indicate temporal variations in the rate of strain release on the Banning strand, or it may indicate missing events in the older section of the trench. In the past 1600 yr, eight paleoearthquakes are documented at both the Burro Flats and Coachella sites, five are documented on the Mission Creek strand at Thousand Palms, and only two are documented on the Banning strand and San Gorgonio Pass fault zone. Given the earthquake ages, a maximum of two earthquakes connecting the Coachella and northern Banning strands is permitted in the past 1600 yr, and only one of these events (ca. 600 CE) could have potentially ruptured onto the San Bernardino strand as well. The interpretation of fewer earthquakes on the Banning strand is consistent with its lower slip rate compared to other sections of the southernmost San Andreas fault and would translate to average slip per event of ~1–5 m.

#### APPENDIX: EARTHQUAKE CHRONOLOGY USING AN ALTERNATIVE AGE MODEL

Figure A1 shows the radiocarbon and luminescence samples used in the alternate age model, and Figure A2 shows the OxCal model for those samples.

#### ACKNOWLEDGMENTS

This research was funded by U.S. Geological Survey (USGS) National Earthquake Hazards Reduction Program grants G18AP00040 and G18AP00041, and internal funding from California State University–San Bernardino (CSUSB) and the USGS. We are extremely grateful to John Rogers for granting access to work on his property and Alan Pace from Petra Geosciences for accommodating our study. We want to thank all the students from CSUSB and California State University–Northridge who assisted with the hard labor. Reviews by Belle Philobosian, Ray Weldon, Peter Gold, and C.H. Jones improved the clarity of the manuscript. The views and conclusions contained in this document are those of the authors and should not be interpreted as necessarily representing the official policies, either expressed or implied, of the U.S. government. Any use of trade, firm, or product names is for descriptive purposes only and does not imply endorsement by the U.S. government.

#### REFERENCES CITED

- Allen, C.R., 1957, San Andreas fault zone in San Gorgonio Pass, Southern California: *Geological Society of America Bulletin*, v. 68, p. 315–350, [https://doi.org/10.1130/0016-7606\(1957\)68\[315:SAFZIS\]2.0.CO;2](https://doi.org/10.1130/0016-7606(1957)68[315:SAFZIS]2.0.CO;2).
- Behr, W.M., Rood, D.H., Fletcher, K.E., Guzman, N., Finkel, R., Hanks, T.C., Hudnut, K.W., Kendrick, K.J., Platt, J.P., Sharp, W.D., Weldon, R.J., and Yule, J.D., 2010, Uncertainties in slip-rate estimates for the Mission Creek strand of the southern San Andreas fault at Biskra Palms Oasis, Southern California: *Geological Society of America Bulletin*, v. 122, p. 1360–1377, <https://doi.org/10.1130/B30020.1>.
- Bevis, M., and Hudnut, K., 2005, B4 Lidar Project: Airborne Laser Swath Mapping (ALSM) Survey of the San Andreas Fault (SAF) System of Central and Southern California, Including the Banning Segment of the SAF and the San Jacinto Fault System: National Center for Airborne Laser Mapping (NCALM), U.S. Geological Survey, the Ohio State University, and the Southern California Integrated GPS Project, distributed by OpenTopography, <https://doi.org/10.5066/F7TQ5ZQ6>.
- Bevis, M., Hudnut, K., Sanchez, R., Toth, C., Grejner-Brzezinska, D., Kendrick, E., Caccamise, D., Raleigh, D., Zhou, H., Shan, S., Shindle, W., Yong, A., Harvey, J., Borsa, A., Ayoub, F., Shrestha,

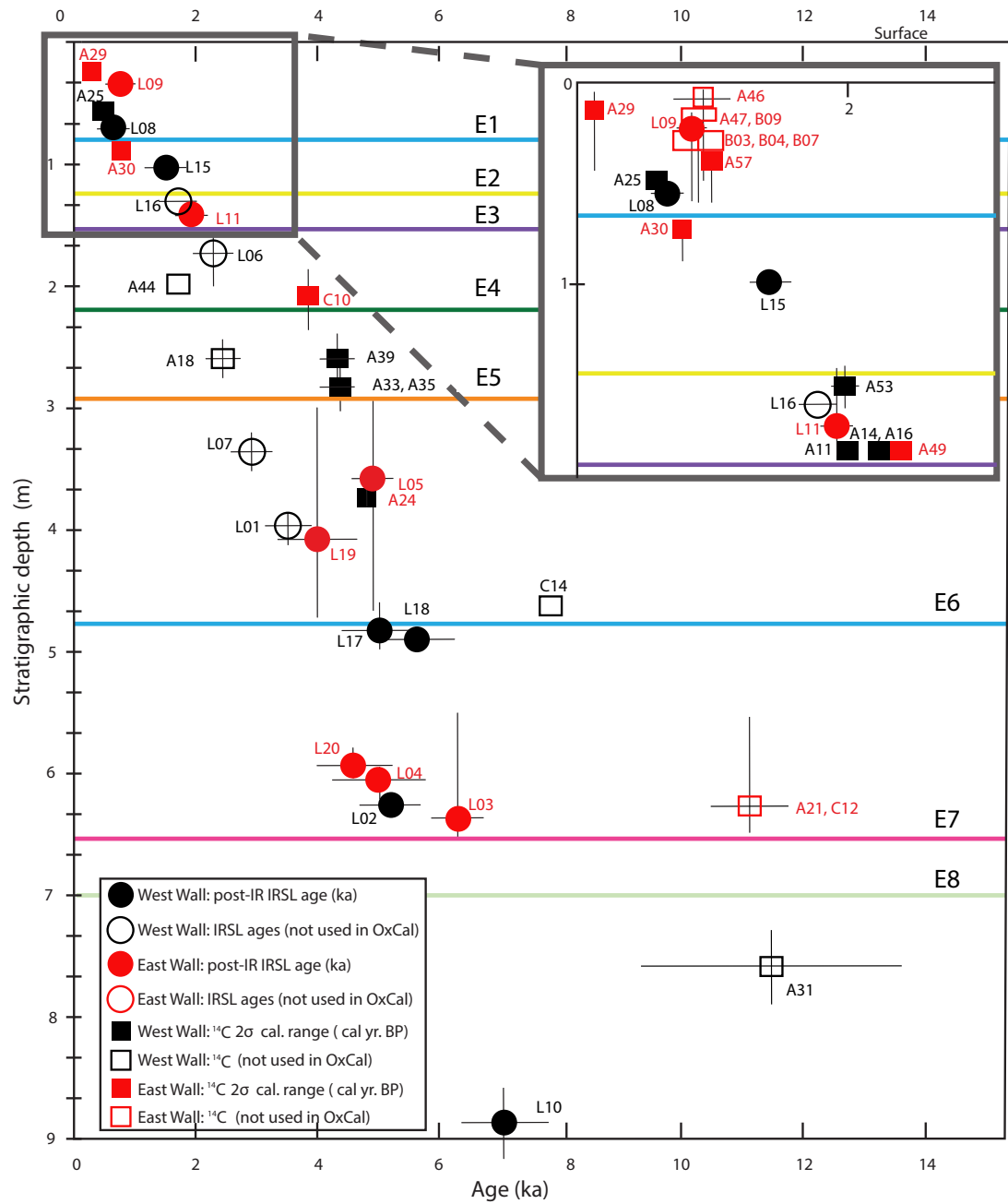


Figure A1. Calibrated radiocarbon and post-infrared infrared stimulated luminescence (post-IR IRSL) ages as a function of stratigraphic depth used in the alternate age model (Fig. A2). Stratigraphic depth was measured on the west wall at 24 m (for layers 20–620) and at 34 m (for layers 620–850). Vertical error bars show uncertainties in correlating sample locations with the type section, and horizontal bars are 2σ errors. Solid symbols show ages that were included in the alternate OxCal model; open symbols show samples excluded from that model.

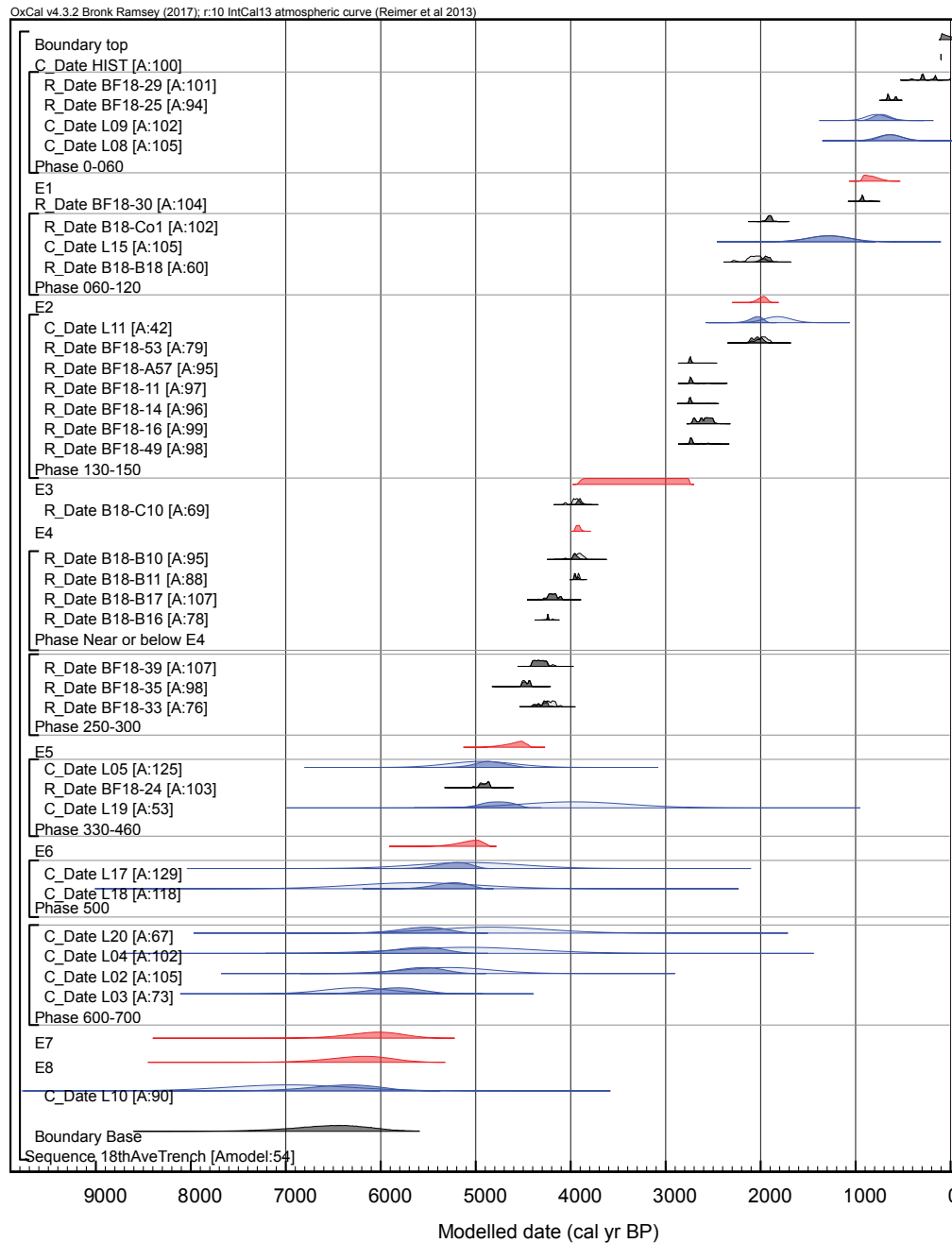


Figure A2. Alternate OxCal model used to estimate earthquake ages, using samples shown in Figure A1. Ages are plotted as a function of stratigraphic position; blue shapes are infrared stimulated luminescence (IRSL) ages, gray shapes are radiocarbon ages, and red shapes are resultant earthquake ages. Brackets indicate samples from the same phase (samples from the same layer or from layers for which the relative stratigraphic position cannot be differentiated). Pale color shows prior probability density functions (PDFs) obtained for the ages of individual samples. Opaque colors are the posterior PDFs for each sample. In this model, we assumed that two samples (A44 and A18) were contaminated by younger material because they are the only radiocarbon samples that produced a 2000 yr spread in layer ages (Fig. 8). These samples were removed first, followed by A31, assuming that the six IRSL samples at the base of the section are correct. To achieve an agreement index >50%, samples L16, L06, L07, and L01 were removed because they are notably younger than both radiocarbon and IRSL samples in the same phase. This model retained 20 of the original radiocarbon and 13 IRSL samples. In comparison to the preferred model, this approach produced much older earthquake ages for E2–E6 (Fig. 10).



- R., Carter, B., Sartori, M., Phillips, D., and Coloma, F., 2005, The B4 project: scanning the San Andreas and San Jacinto fault zones: Abstract H34B-01 presented at 2005 Fall Meeting, AGU, San Francisco, California, December.
- Blisniuk, K., Scharer, K., Sharp, W.D., Burgmann, R., Amos, C., and Rymer, M., 2021, A revised position for the primary strand of the Pleistocene-Holocene San Andreas fault in southern California: *Science Advances*, v. 7, 14 p.
- Bonilla, M.G., and Lienkaemper, J.J., 1991, Factors Affecting the Recognition of Faults Exposed in Exploratory Trenches: U.S. Geological Survey Bulletin 1947, 54 p., <https://doi.org/10.3133/b1947>.
- Bøtter-Jensen, L., Andersen, C., Duller, G., and Murray, A., 2003, Developments in radiation, stimulation and observation facilities in luminescence measurements: *Radiation Measurements*, v. 37, p. 535–541, [https://doi.org/10.1016/S1350-4487\(03\)00020-9](https://doi.org/10.1016/S1350-4487(03)00020-9).
- Brennan, B.J., Lyons, R.G., and Phillips, S.W., 1991, Attenuation of alpha particle track dose for spherical grains: *International Journal of Radiation Applications and Instrumentation, Part D, Nuclear Tracks and Radiation Measurements*, v. 18, p. 249–253, [https://doi.org/10.1016/1359-0189\(91\)90119-3](https://doi.org/10.1016/1359-0189(91)90119-3).
- Bronk Ramsey, C., 2009, Bayesian analysis of radiocarbon dates: *Radiocarbon*, v. 51, p. 337–360, <https://doi.org/10.1017/S0033822200033865>.
- Bronk Ramsey, C., 2017, Methods for summarizing radiocarbon datasets: *Radiocarbon*, v. 59, p. 1809–1833, <https://doi.org/10.1017/RDC.2017.108>.
- Buylaert, J., Murray, A., Thomsen, K., and Jain, M., 2009, Testing the potential of an elevated temperature IRSL signal from K-feldspar: *Radiation Measurements*, v. 44, p. 560–565, <https://doi.org/10.1016/j.radmeas.2009.02.007>.
- Cardona, J., 2016, Constraining the Most Recent Surface Rupture on the Garnet Hill Strand, San Andreas Fault, Coachella Valley, California [Master's thesis]: Northridge, California, California State University, 79 p.
- Douilly, R., Oglesby, D.D., Cooke, M.L., and Hatch, J.L., 2020, Dynamic models of earthquake rupture along branch faults of the eastern San Geronio Pass region in California using complex fault structure: *Geosphere*, v. 16, no. 2, p. 474–489, <https://doi.org/10.1130/GES02192.1>.
- Durcan, J.A., King, G.E., and Duller, G.A.T., 2015, DRAC: Dose Rate and Age Calculator for trapped charge dating: *Quaternary Geochronology*, v. 28, p. 54–61, <https://doi.org/10.1016/j.quageo.2015.03.012>.
- Fletcher, K.E.K., Sharp, W.D., Kendrick, K.J., Behr, W.M., Hudnut, K.W., and Hanks, T.C., 2010, <sup>230</sup>Th/U dating of a late Pleistocene alluvial fan along the southern San Andreas fault: *Geological Society of America Bulletin*, v. 122, p. 1347–1359, <https://doi.org/10.1130/B30018.1>.
- Fosdick, J.C., and Blisniuk, K., 2018, Sedimentary signals of recent faulting along an old strand of the San Andreas fault, USA: *Scientific Reports*, v. 8, p. 12132, <https://doi.org/10.1038/s41598-018-30622-3>.
- Fuis, G.S., Klaus, B., Goldman, M.R., Ryberg, T., and Langenheim, V.E., 2017, Subsurface geometry of the San Andreas fault in Southern California: Results from the Salton Seismic Imaging Project (SSIP) and strong ground motion expectation: *Bulletin of the Seismological Society of America*, v. 107, no. 4, p. 1642–1662, <https://doi.org/10.1785/0120160309>.
- Fumal, T.E., Rymer, M.J., and Seitz, G.G., 2002, Timing of large earthquakes since A.D. 800 on the Mission Creek strand of the San Andreas fault zone at Thousand Palms Oasis, near Palm Springs, California: *Bulletin of the Seismological Society of America*, v. 92, no. 7, p. 2841–2860, <https://doi.org/10.1785/0120000609>.
- Galbraith, R.F., Roberts, R.G., Laslett, G.M., Yoshida, H., and Olley, J.M., 1999, Optical dating of single and multiple grains of quartz from Jinnium rock shelter, northern Australia: Part I. Experimental design and statistical models: *Archaeometry*, v. 41, p. 339–364, <https://doi.org/10.1111/j.1475-4754.1999.tb00987.x>.
- Gold, P.O., Behr, W.M., Rood, D., Kendrick, K., Rockwell, T.K., and Sharp, W.D., 2015, Holocene geologic slip rate for the Banning strand of the southern San Andreas fault near San Geronio Pass: *Journal of Geophysical Research—Solid Earth*, v. 120, no. 8, p. 5639–5663, <https://doi.org/10.1002/2015JB012004>.
- Guerin, G., Mercier, N., Nathan, R., Adamiec, C., and Lefrais, Y., 2012, On the use of the infinite matrix assumption and associated concepts: A critical review: *Radiation Measurements*, v. 47, p. 778–785, <https://doi.org/10.1016/j.radmeas.2012.04.004>.
- Heermance, R.V., and Yule, J.D., 2017, Holocene slip rates along the San Andreas fault system in the San Geronio Pass and implications for large earthquakes in Southern California: *Geophysical Research Letters*, v. 44, no. 11, p. 5391–5400, <https://doi.org/10.1002/2017GL072612>.
- Huntley, D.J., and Baril, M.R., 1997, The K content of the K-feldspars being measured in optical dating or in thermoluminescence dating: *Ancient TL*, v. 15, p. 11–13.
- Huntley, D.J., and Lamothe, M., 2001, Ubiquity of anomalous fading in K-feldspars and the measurement and correction for it in optical dating: *Canadian Journal of Earth Sciences*, v. 38, p. 1093–1106, <https://doi.org/10.1139/e01-013>.
- Jones, L.M., Bernkopf, R., Cox, D., Goltz, J., Hudnut, K., Mileti, D., Perry, S., Ponti, D., Porter, K., Reichle, M., Seligson, H., Shoaf, K., Treiman, J., and Wein, A., 2008, The ShakeOut Scenario: U.S. Geological Survey Open-File Report 2008–1150 and California Geological Survey Preliminary Report 25, 312 p., <http://pubs.usgs.gov/of/2008/1150>.
- Kendrick, K.J., Matti, J.C., and Mahan, S.A., 2015, Late Quaternary slip history of the Mill Creek strand of the San Andreas fault in San Geronio Pass, Southern California: The role of a subsidiary left-lateral fault in strand switching: *Geological Society of America Bulletin*, v. 127, no. 5–6, p. 825–849, <https://doi.org/10.1130/B31101.1>.
- Kreutzer, S., Schmidt, C., Fuchs, M., Dietze, M., Fischer, M., and Fuchs, M., 2012, Introducing an R package for luminescence dating analysis: *Ancient TL*, v. 30, p. 1–8.
- Lancaster, J.T., Hayhurst, C.A., and Bedrossian, T.L., compilers, 2012, Preliminary Geologic Map of Quaternary Superficial Deposits in Southern California Palm Springs 30' x 60' Quadrangle: California Geological Survey Special Report 217, Plate 24, scale 1:100,000.
- Lienkaemper, J.J., and Bronk Ramsey, C., 2009, OxCal: Versatile tool for developing paleoearthquake chronologies; a primer: *Seismological Research Letters*, v. 80, no. 3, p. 431–434, <https://doi.org/10.1785/gssrl.80.3.431>.
- Liritzis, I., Stamoulis, K., Papachristodoulou, C., and Ioannides, K., 2013, A re-evaluation of radiation dose rate conversion factors: *Mediterranean Archaeology and Archaeometry*, v. 13, p. 1–15.
- Matti, J.C., and Morton, D.M., 1993, Paleogeographic evolution of the San Andreas fault in southern California: A reconstruction based on a new cross-fault correlation, *in* Powell, R.E., Weldon, R.E., II, and Matti, J.C., eds., *The San Andreas Fault System: Displacement, Palinspastic Reconstruction, and Geologic Evolution*: Geological Society of America Memoir 178, p. 107–160, <https://doi.org/10.1130/MEM178-p107>.
- Matti, J.C., Morton, D.M., and Cox, B.F., 1985, Distribution and Geologic Relations of Fault Systems in the Vicinity of the Central Transverse Ranges, Southern California: U.S. Geological Survey Open-File Report 85-365, 27 p., scale 1:250,000.
- McCaffrey, R., 2005, Block kinematics of the Pacific–North America plate boundary in the southwestern United States from inversion of GPS, seismological, and geologic data: *Journal of Geophysical Research*, v. 110, B07401, <https://doi.org/10.1029/2004JB003307>.
- McGill, S.F., and Rubin, C.M., 1999, Surficial slip distribution on the central Emerson fault during the June 28, 1992, Landers earthquake, California: *Journal of Geophysical Research*, v. 104, p. 4811–4833, <https://doi.org/10.1029/98JB01556>.
- McGill, S.F., Dergham, S., Barton, K., Berney-Ficklin, T., Grant, D., Hartling, C., Hobart, K., Minnich, R., Rodriguez, M., Runnerstorm, E., Russell, J., Schmoker, K., Stumfall, M., Townsend, J., and Williams, J., 2002, Paleoseismology of the San Andreas fault at Plunge Creek, near San Bernardino, southern California: *Bulletin of the Seismological Society of America*, v. 92, p. 2803–2840, <https://doi.org/10.1785/0120000607>.
- McGill, S.F., Spinler, J.C., McGill, J.D., Bennett, R.A., Floyd, M., Fryxell, J.E., and Funning, G.J., 2015, Kinematic modeling of fault slip rates using new geodetic velocities from a transect across the Pacific–North America plate boundary through the San Bernardino Mountains, California: *Journal of Geophysical Research*, v. 120, p. 2772–2793, <https://doi.org/10.1002/2014JB011459>.
- Meade, B.J., and Hager, B.H., 2005, Block models of crustal motion in southern California constrained by GPS measurements: *Journal of Geophysical Research*, v. 110, B03403, <https://doi.org/10.1029/2004JB003209>.
- Nicholson, C., 1996, Seismic behavior of the southern San Andreas fault zone in the northern Coachella Valley, California: Comparison of the 1948 and 1986 earthquake sequences: *Bulletin of the Seismological Society of America*, v. 86, no. 5, p. 1331–1349.
- Nur, A., Ron, H., and Beroza, G.C., 1993, The nature of the Landers-Mojave earthquake line: *Science*, v. 261, no. 5118, p. 201–203, <https://doi.org/10.1126/science.261.5118.201>.
- Onderdonk, N., McGill, S., and Rockwell, T., 2018, A 3700 yr paleoseismic record from the northern San Jacinto fault and implications for joint rupture of the San Jacinto and San Andreas faults: *Geosphere*, v. 14, p. 2447–2468, <https://doi.org/10.1130/GES01687.1>.
- Philibosian, B., Fumal, T.E., and Weldon, R.J., 2011, San Andreas fault earthquake chronology and Lake Cahuilla history at Coachella, California: *Bulletin of the Seismological Society of America*, v. 101, no. 1, p. 13–38, <https://doi.org/10.1785/0120100050>.

- Prescott, J.R., and Hutton, J.T., 1994, Cosmic ray contributions to dose rates for luminescence and ESR dating: Large depths and long-term time variations: *Radiation Measurements*, v. 23, p. 497–500, [https://doi.org/10.1016/1350-4487\(94\)90086-8](https://doi.org/10.1016/1350-4487(94)90086-8).
- Reimer, P.J., Bard, E., Bayliss, A., Beck, J.W., Blackwell, P.G., Ramsey, C.B., Buck, C.E., Cheng, H., Edwards, R.L., Friedrich, M., Grootes, P.M., Guilderson, T.P., Hafliðason, H., Hajdas, I., et al., 2013, IntCal13 and Marine13 radiocarbon age calibration curves 0–50,000 years cal BP: *Radiocarbon*, v. 55, p. 1869–1887, [https://doi.org/10.2458/azu\\_js\\_rc.55.16947](https://doi.org/10.2458/azu_js_rc.55.16947).
- Rhodes, E., 2015, Dating sediments using potassium feldspar single-grain IRSL: Initial methodological considerations: *Quaternary International*, v. 362, p. 14–22, <https://doi.org/10.1016/j.quaint.2014.12.012>.
- Rockwell, T.K., Meltzner, A.J., and Haaker, E.C., 2018, Dates of the two most recent surface ruptures on the southernmost San Andreas fault recalculated by precise dating of Lake Cahuilla dry periods: *Bulletin of the Seismological Society of America*, v. 108, p. 2634–2649, <https://doi.org/10.1785/0120170392>.
- Rymer, M.J., 1997, Structural link between the San Andreas fault and the Eastern California shear zone, Coachella Valley and Little San Bernardino Mountains, Southern California: *Geological Society of America Abstracts with Programs*, v. 29, no. 5, p. 61–62.
- Scharer, K.M., and Yule, D., 2020, A maximum rupture model for the southern San Andreas and San Jacinto faults, California, derived from paleoseismic earthquake ages: Observations and limitations: *Geophysical Research Letters*, v. 47, no. 15, e2020GL088532, <https://doi.org/10.1029/2020GL088532>.
- Scharer, K., Blisniuk, K., Sharp, W., and Mudd, S.M., 2016, Slip transfer and the growth of the Indio and Edom Hills, southern San Andreas fault: *Geological Society of America Abstracts with Programs*, v. 48, no. 4, abstract 14-3, <https://doi.org/10.1130/abs/2016CD-274217>.
- Scharer, K.R., Weldon, I.I., Biasi, G., Streig, A., and Fumal, T., 2017, Ground-rupturing earthquakes on the northern Big Bend of the San Andreas fault, California, 800 A.D. to present: *Journal of Geophysical Research—Solid Earth*, v. 122, p. 2193–2218, <https://doi.org/10.1002/2016JB013606>.
- Schieleln, P., and Lomax, J., 2013, The effect of fluvial environments on sediment bleaching and Holocene luminescence ages—A case study from the German alpine foreland: *Geochronometria*, v. 40, p. 283–293, <https://doi.org/10.2478/s13386-013-0120-y>.
- Sharp, R.V., Rymer, M.J., and Morton, D.M., 1986, Trace-fractures on the Banning fault created in association with the 1986 North Palm Springs earthquake: *Bulletin of the Seismological Society of America*, v. 76, no. 6, p. 1838–1843.
- Sieh, K.E., and Williams, P.L., 1990, Behavior of the southernmost San Andreas fault during the past 300 years: *Journal of Geophysical Research*, v. 95, p. 6629–6645, <https://doi.org/10.1029/JB095iB05p06629>.
- Spinler, J.C., Bennett, R.A., Anderson, M.L., McGill, S.F., Hreinsdóttir, S., and McCallister, A., 2010, Present-day strain accumulation and slip rates associated with southern San Andreas and Eastern California shear zone faults: *Journal of Geophysical Research*, v. 115, B11407, <https://doi.org/10.1029/2010JB007424>.
- Stuiver, M., and Polach, H., 1977, Discussion: Reporting of  $^{14}\text{C}$  data: *Radiocarbon*, v. 19, p. 355–363, <https://doi.org/10.1017/S0033822200003672>.
- Toppozada, T.R., Branum, D.M., Reichle, M.S., and Hallstrom, C.L., 2002, San Andreas fault zone, California:  $M \geq 5.5$  earthquake history: *Bulletin of the Seismological Society of America*, v. 92, no. 7, p. 2555–2601, <https://doi.org/10.1785/0120000614>.
- U.S. Geological Survey and California Geological Survey, 2018, Quaternary Fault and Fold Database for the United States: U.S. Geological Survey, <https://www.usgs.gov/natural-hazards/earthquake-hazards/faults> (accessed May 2020).
- Weldon, R.J., II, Fumal, T.E., Powers, T.J., Pezzopane, S.K., Scharer, K.M., and Hamilton, J.C., 2002, Structure and earthquake offsets on the San Andreas faults at the Wrightwood, California, paleoseismic site: *Bulletin of the Seismological Society of America*, v. 92, no. 7, p. 2704–2725, <https://doi.org/10.1785/0120000612>.
- Wesnousky, S.G., 2008, Displacement and geometrical characteristics of earthquake surface ruptures: Issues and implications for seismic-hazard analysis and the process of earthquake rupture: *Bulletin of the Seismological Society of America*, v. 98, no. 4, p. 1609–1632, <https://doi.org/10.1785/0120070111>.
- Williams, P.L., McGill, S.F., Sieh, K.E., Allen, C.R., and Louie, J.N., 1988, Triggered slip along the San Andreas fault after the 8 July 1986 North Palm Springs earthquake: *Bulletin of the Seismological Society of America*, v. 78, p. 1112–1122.
- Wintle, A., and Murray, A., 2006, A review of quartz optically stimulated luminescence characteristics and their relevance in single-aliquot regeneration dating protocols: *Radiation Measurements*, v. 41, p. 369–391, <https://doi.org/10.1016/j.radmeas.2005.11.001>.
- Wolff, L., 2018, 6000-Year Record of Large, Infrequent Earthquakes on the San Andreas Fault System in San Geronio Pass, near Cabazon, California [Master's thesis]: Northridge, California, California State University, 106 p.
- Yule, J.D., and Sieh, K., 2003, Complexities of the San Andreas fault near San Geronio Pass: Implications for large earthquakes: *Journal of Geophysical Research*, v. 108, no. B11, p. ETG 9-1–9-23, <https://doi.org/10.1029/2001JB000451>.
- Yule, J.D., Maloney, S.J., Cummings, L.S., Prentice, C., Ellsworth, W., and Hellweg, P., 2006, Using pollen to constrain the age of the youngest rupture of the San Andreas fault at San Geronio Pass: *Seismological Research Letters*, v. 77, no. 2, p. 245.